

# A Stochastic Projection Method for Fluid Flow

## II. Random Process

Olivier P. Le Maître,\* Matthew T. Reagan,† Habib N. Najm,‡  
Roger G. Ghanem,‡ and Omar M. Knio§<sup>1</sup>

\**Centre d'Etudes de Mécanique d'Ile de France, Université d'Evry Val d'Essone, 40 rue du Pelvoux, 91020 Evry cedex, France;* †*Combustion Research Facility, Sandia National Laboratories, Livermore, California 94550;* ‡*Department of Civil Engineering, The Johns Hopkins University, Baltimore, Maryland 21218-2686;* and §*Department of Mechanical Engineering, The Johns Hopkins University, Baltimore, Maryland 21218-2686*  
E-mail: olm@iup.univ-evry.fr, mtreaga@ca.sandia.gov, hnnajm@ca.sandia.gov, ghanem@jhu.edu, and knio@jhu.edu

Received October 1, 2001; revised May 1, 2002

---

An uncertainty quantification scheme is developed for the simulation of stochastic thermofluid processes. The scheme relies on spectral representation of uncertainty using the polynomial chaos (PC) system. The solver combines a Galerkin procedure for the determination of PC coefficients with a projection method for efficiently simulating the resulting system of coupled transport equations. Implementation of the numerical scheme is illustrated through simulations of natural convection in a 2D square cavity with stochastic temperature distribution at the cold wall. The properties of the uncertainty representation scheme are analyzed, and the predictions are contrasted with results obtained using a Monte Carlo approach. © 2002 Elsevier Science (USA)

*Key Words:* stochastic; natural convection; Navier-Stokes; polynomial chaos; Karhunen–Loève; uncertainty.

---

### 1. INTRODUCTION

Uncertainty propagation and quantification can be an essential step in the development of complex models, in particular when these models involve inexact knowledge of system forcing or system parameters. This article is part of an effort that aims at developing uncertainty quantification schemes for fluid systems involving transport and chemistry.

As an initial step toward these objectives, a stochastic projection method (SPM) was developed in a previous work [1]. In [1] attention was focused on an incompressible flow model,

<sup>1</sup> Corresponding author.

where uncertain model data are generated by a single random variable. SPM combines a projection method for fluid flow with a spectral representation of the effect of uncertainty in terms of the polynomial chaos (PC) system [2–9]. The objectives of the present effort are twofold: (1) to extend the capabilities of SPM to situations involving random processes, and (2) to generalize the underlying formulation so as to account for weak compressibility effects. To illustrate the development, we focus on natural convection in an enclosed cavity. This topic has received considerable attention in the recent literature and various approaches have been proposed, including models based on the well-known Boussinesq approximation (e.g., [10–12]) as well as low-Mach-number models (e.g., [13, 14]). In addition, simulations of internal natural convection have been used as benchmark tests for different flow regimes [10, 15–27].

In one of its simplest forms, the problem consists of a square or rectangular cavity with adiabatic horizontal boundaries and differentially but uniformly heated vertical walls. In practice, however, this idealized situation may be difficult to achieve, for instance due to imperfections in insulation and/or nonuniform heating and cooling. Computed solutions are often very sensitive to applied boundary conditions, which can complicate comparison with experimental measurements [28].

The present effort aims at generalizing the previous construction [1] along two directions, namely, by considering flows with (small) temperature and density gradients and by considering uncertain model data associated with a random process. Motivated in part by the aforementioned observations, we focus on the idealized case of natural convection in a square cavity under stochastic boundary conditions. As outlined in Section 2, we restrict the study to natural convection in the Boussinesq limit. A stochastic formulation is then introduced in Section 3 which consists of treating the hot wall as having a uniform temperature and imposing a stochastic temperature distribution on the cold vertical boundary. The latter is treated as a Gaussian process characterized by its variance and correlation length. The Karhunen–Loève expansion [29] is then applied to construct an efficient representation of this process and to generalize the PC representation used in the previous version of SPM [1]. A brief validation study of the deterministic prediction is first performed in Section 5 and is used to select an appropriate grid resolution level. The convergence properties of the spectral stochastic scheme are then analyzed in Section 6, and the properties of the computed velocity and temperature modes are examined in Section 7. To verify the spectral computations, a nonintrusive spectral projection (NISP) approach is introduced and applied in Section 8. The essential idea in NISP is to use deterministic predictions to determine the stochastic response of the system. Two variants are considered, one based on high-order Gauss–Hermite (GH) quadrature [30, 31] and the other on Latin hypercube sampling (LHS) strategy [32]. The predictions of both sampling schemes are contrasted with the spectral computations and are used to further examine its properties. In Section 9, a quantitative analysis of the effects of the imposed stochastic temperature profile is provided. Major conclusions are summarized in Section 10.

## 2. DETERMINISTIC FORMULATION

We consider a square 2D cavity, of side  $L_e$ , filled with a Newtonian fluid of density  $\rho$ , molecular viscosity  $\mu$ , and thermal conductivity  $\kappa$ . The coordinate system is chosen so that  $y$  is the vertical direction, pointing upward, and the  $x$  axis is horizontal. The two horizontal walls are assumed to be adiabatic. The left vertical wall is maintained at uniform

temperature  $T_h$ , and the right vertical wall is maintained at  $T_c$ . We assume that  $T_h > T_c$ , so that the left vertical wall (located at  $x = 0$ ) is referred to as the hot wall, while the right vertical wall is the cold wall.

In the Boussinesq limit,  $2(T_h - T_c)/(T_h + T_c) \ll 1$ , the normalized governing equations are expressed as [12]

$$\frac{\partial \mathbf{u}}{\partial t} + \mathbf{u} \cdot \nabla \mathbf{u} = -\nabla p + \frac{Pr}{\sqrt{Ra}} \nabla^2 \mathbf{u} + Pr \theta \mathbf{e}_y, \quad (1)$$

$$\nabla \cdot \mathbf{u} = 0, \quad (2)$$

$$\frac{\partial \theta}{\partial t} + \nabla \cdot (\mathbf{u} \theta) = \frac{1}{\sqrt{Ra}} \nabla^2 \theta, \quad (3)$$

where  $\mathbf{u}$  is the velocity,  $t$  is time,  $p$  is pressure,  $\mathbf{e}_y$  is the unit vector in the vertical  $y$  direction, and  $\theta \equiv (T - T_{\text{ref}})/\Delta T_{\text{ref}}$  is the normalized temperature. The reference temperature  $T_{\text{ref}} \equiv (T_h + T_c)/2$  and the reference temperature difference  $\Delta T_{\text{ref}} \equiv T_h - T_c$ . Unless otherwise noted, variables are normalized with respect to the appropriate combination of reference length  $L_c$ , velocity  $V$ , time  $\tau \equiv L_c/V$ , and pressure  $P = \rho V^2$ . The normalization leads to the usual definitions of Prandtl and Rayleigh numbers, respectively  $Pr = \mu c_p/\kappa$  and  $Ra = \rho g \beta \Delta T_{\text{ref}} L_c^3/(\mu \kappa)$ , where  $\beta$  is the coefficient of thermal expansion and  $g$  is gravitational acceleration. In all cases, the deterministic system is integrated from an initial state of rest using  $Pr = 0.71$  and  $Ra = 10^6$ . For this choice of physical parameters, a steady, laminar recirculating flow regime occurs [12].

### 3. STOCHASTIC FORMULATION

We consider the effect of ‘‘random’’ fluctuations on the cold wall. The normalized mean wall temperature at  $x = 1$  is expressed as

$$\theta_1(y) \equiv \theta(x = 1, y) = \theta_c + \theta'(y) = -\frac{1}{2} + \theta'(y). \quad (4)$$

Using angle brackets to denote expectations, we have  $\langle \theta_1 \rangle = \theta_c$ ; i.e.,  $\theta'$  has vanishing expectation and the mean (dimensional) temperature along the cold wall is independent of  $y$  and equals  $T_c$ .

The random component is assumed to be given by a Gaussian process which is characterized by its variance  $\sigma_\theta^2$  and an autocorrelation function  $\mathcal{K}$  given by

$$\mathcal{K}(y_1, y_2) \equiv \mathcal{K}(|y_1 - y_2|) \equiv \langle \theta'(y_1) \theta'(y_2) \rangle = \sigma_\theta^2 \exp[-|y_1 - y_2|/L_c], \quad (5)$$

where  $L_c$  is the normalized correlation length.  $\mathcal{K}$  can be expanded in terms of its eigenvalues,  $\lambda_i$ , and eigenfunctions,  $f_i(y)$ , using [9, 33, 34]

$$\mathcal{K}(y_1, y_2) = \sum_{i=0}^{\infty} \lambda_i f_i(y_1) f_i(y_2), \quad (6)$$

and  $\theta'$  can be accordingly expressed in the usual Karhunen–Loève (KL) expansion as [29]

$$\theta'(y) = \sum_{i=0}^{\infty} \sqrt{\lambda_i} f_i(y) \xi_i, \quad (7)$$

where the  $\xi_i$ 's are uncorrelated Gaussian variables having vanishing expectation and unit variance.

The eigenvalues and eigenfunctions of  $\mathcal{K}$  are solutions of the corresponding integral operator [9, 33, 34],

$$\int_0^1 \mathcal{K}(y_1, y_2) f(y_2) dy_2 = \lambda f(y_1). \quad (8)$$

This Fredholm equation can be solved numerically, but an analytical solution for the kernel in Eq. (5) is available [9] and is given by

$$f_n(y) = \begin{cases} \frac{\cos[\omega_n(y - 1/2)]}{\sqrt{\frac{1}{2} + \frac{\sin(\omega_n)}{2\omega_n}}} & \text{if } n \text{ is even,} \\ \frac{\sin[\omega_n(y - 1/2)]}{\sqrt{\frac{1}{2} - \frac{\sin(\omega_n)}{2\omega_n}}} & \text{if } n \text{ is odd,} \end{cases} \quad (9)$$

where

$$\lambda_n = \sigma_\theta^2 \frac{2L_c}{1 + (\omega_n L_c)^2}, \quad (10)$$

and  $\omega_n$  are the positive (ordered) roots of the characteristic equation

$$[1 - L_c \omega \tan(\omega/2)][L_c \omega + \tan(\omega/2)] = 0. \quad (11)$$

Since the first positive root of Eq. (11) is  $\omega_0 = 0$ , corresponding to  $f_0 = 0$ , Eq. (7) may be rewritten as

$$\theta'(y) = \sum_{i=1}^{\infty} \xi_i \sqrt{\lambda_i} f_i(y). \quad (12)$$

Figure 1 depicts the first 10 eigenvalues and eigenfunctions for a process with  $L_c = 1$ . Note that as the index increases, the eigenfunctions exhibit higher frequencies while the corresponding eigenvalues decrease. As discussed in [9] the decay rate of the spectrum increases with decreasing  $L_c$ .

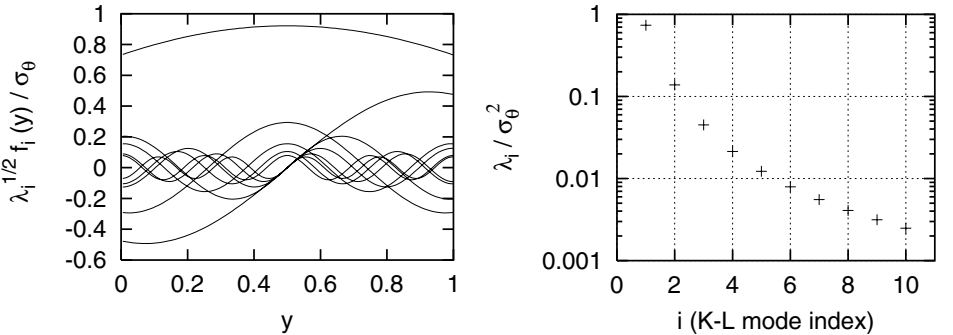


**FIG. 1.** Karhunen–Loève expansion for the temperature fluctuation  $\theta'(y)$  corresponding to an exponential correlation function with characteristic length  $L_c = 1$ . In the left plot, the first ten mode shapes ( $\sqrt{\lambda_i} f_i(y)$ ) are reported. The right plot shows the eigenvalues  $\lambda_i$ . The quantities have been respectively normalized using  $\sigma_\theta$  and  $\sigma_\theta^2$ .

**TABLE I**  
 $E_\sigma^2$  and  $E_\sigma^\infty$  for Various Values of  $N_{\text{KL}}$  for  $L_c = 1/2, 1, \text{ and } 2$

	$N_{\text{KL}}$				
	4	6	10	20	40
$E_\sigma^2(N_{\text{KL}}) - L_c = 1/2$	0.5882E-1	0.3751E-1	0.2161E-1	0.1045E-1	0.5129E-2
$E_\sigma^2(N_{\text{KL}}) - L_c = 1$	0.2947E-1	0.1871E-1	0.1077E-1	0.5213E-2	0.2562E-2
$E_\sigma^2(N_{\text{KL}}) - L_c = 2$	0.1473E-1	0.9337E-2	0.5376E-2	0.2604E-2	0.1280E-2
$E_\sigma^\infty(N_{\text{KL}}) - L_c = 1/2$	0.1076E-0	0.6592E-1	0.3453E-1	0.1300E-1	0.5590E-2
$E_\sigma^\infty(N_{\text{KL}}) - L_c = 1$	0.5346E-1	0.3255E-1	0.1704E-1	0.6429E-2	0.2792E-2
$E_\sigma^\infty(N_{\text{KL}}) - L_c = 2$	0.2657E-1	0.1615E-1	0.8456E-2	0.3197E-2	0.1395E-2

In numerical implementations, the KL expansion [Eq. (12)] is truncated, and the temperature “fluctuation” is approximated as

$$\theta' = \sum_{i=1}^{N_{\text{KL}}} \xi_i \sqrt{\lambda_i} f_i(y), \quad (13)$$

where  $N_{\text{KL}}$  is the number of modes retained in the computations. The error introduced by this truncation is quantified in terms of the  $L_p$  norms:

$$E_{\mathcal{K}}^p(N_{\text{KL}}) = \left[ \int_0^1 \int_0^1 \left| \mathcal{K}(y_1, y_2) - \sum_{i=1}^{N_{\text{KL}}} \lambda_i f_i(y_1) f_i(y_2) \right|^p dy_1 dy_2 \right]^{1/p}, \quad (14)$$

$$E_\sigma^p(N_{\text{KL}}) = \left[ \int_0^1 \left| \sigma_\theta - \sqrt{\sum_{i=1}^{N_{\text{KL}}} \lambda_i f_i^2(y)} \right|^p dy \right]^{1/p}. \quad (15)$$

Table I reports  $E_\sigma^2$  and  $E_\sigma^\infty$  for different values of  $N_{\text{KL}}$  and for  $L_c = 1/2, 1, \text{ and } 2$ ; Table II provides the corresponding values of  $E_{\mathcal{K}}^2$  and  $E_{\mathcal{K}}^\infty$ . The results indicate that at fixed  $N_{\text{KL}}$  the “truncation” errors scale approximately as  $1/L_c$ . At fixed correlation length,  $E_\sigma^2$  and  $E_{\mathcal{K}}^\infty$  decrease as  $N_{\text{KL}}^1$ , while  $E_\sigma^\infty$  and  $E_{\mathcal{K}}^2$  exhibit faster decay rates. The effect of truncation of  $\mathcal{K}$  is further illustrated in Fig. 2, which depicts the truncated correlation function and its deviation from the exact solution for  $L_c = 1$ . The results indicate that the truncation error is mainly concentrated in a thin band around the axis  $y_1 = y_2$  and that it exhibits rapid

**TABLE II**  
 $E_{\mathcal{K}}^2$  and  $E_{\mathcal{K}}^\infty$  for Various Values of  $N_{\text{KL}}$  for  $L_c = 1/2, 1, \text{ and } 2$

	$N_{\text{KL}}$				
	4	6	10	20	40
$E_{\mathcal{K}}^2(N_{\text{KL}}) - L_c = 1/2$	0.3366E-1	0.1791E-1	0.8176E-2	0.2988E-2	0.1249E-2
$E_{\mathcal{K}}^2(N_{\text{KL}}) - L_c = 1$	0.1736E-1	0.9076E-2	0.4107E-2	0.1496E-2	0.6247E-3
$E_{\mathcal{K}}^2(N_{\text{KL}}) - L_c = 2$	0.8789E-2	0.4562E-2	0.2057E-2	0.7882E-3	0.3124E-3
$E_{\mathcal{K}}^\infty(N_{\text{KL}}) - L_c = 1/2$	0.2188E-0	0.1439E-0	0.8462E-1	0.4149E-1	0.2051E-1
$E_{\mathcal{K}}^\infty(N_{\text{KL}}) - L_c = 1$	0.1127E-0	0.7285E-1	0.4250E-1	0.2076E-1	0.1026E-1
$E_{\mathcal{K}}^\infty(N_{\text{KL}}) - L_c = 2$	0.5699E-1	0.3660E-1	0.2128E-1	0.1039E-1	0.5130E-2

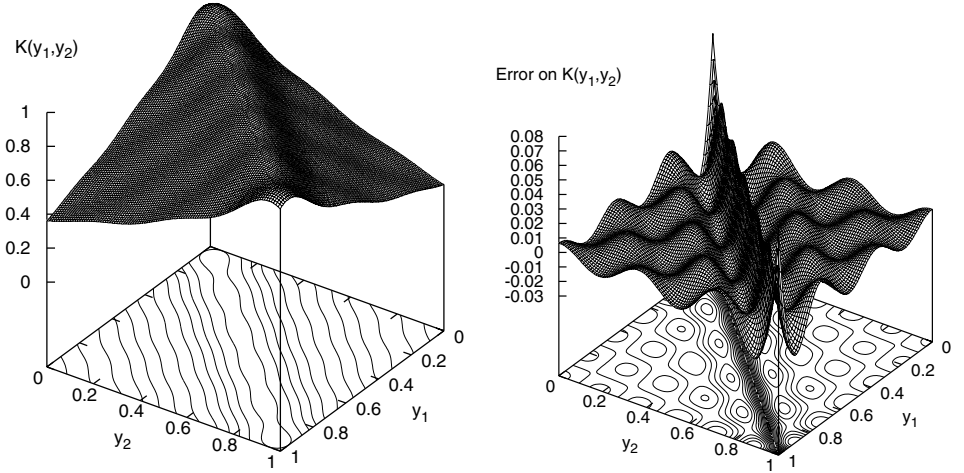


**FIG. 2.** Truncated correlation function  $\mathcal{K}(y_1, y_2)$  (left) and its deviation from the exact value (right). An exponential autocorrelation function is used with  $L_c = 1$ . The truncation is at  $N_{\text{KL}} = 6$ .

oscillatory decay as one moves away from the axis. It thus appears that the truncation, which removes the highest frequency modes, primarily affects the short-scale correlations. The truncated modes are expected to have a weak influence on the solution and this is in fact reflected in the analysis that follows, which indicates that a modest number of KL modes is generally sufficient.

#### 4. SPECTRAL STOCHASTIC REPRESENTATION

As in [1], the dependence of the solution on the uncertain model data is represented in terms of the PC system. We illustrate this representation for generic field variable,  $\Phi(\mathbf{x}, t, \boldsymbol{\xi})$ , where  $\boldsymbol{\xi} = \xi_1, \dots, \xi_{N_{\text{KL}}}$ .  $\Phi$  is decomposed according to

$$\Phi(\mathbf{x}, t, \boldsymbol{\xi}) = \sum_{i=0}^P \Phi_i(\mathbf{x}, t) \Psi_i(\boldsymbol{\xi}), \quad (16)$$

where  $\Phi_i$  are (yet to be determined) deterministic “coefficients,”  $\Psi_i$  denote the polynomial chaos [2, 3, 29], while  $P + 1$  is the total number of modes used in the spectral expansion. Note that the  $\Psi_i$  are multidimensional orthogonal polynomials of the uncorrelated Gaussians, and that for  $i = 1, \dots, N_{\text{KL}}$ ,  $\Psi_i(\boldsymbol{\xi}) = \xi_i$ ; i.e., these  $N_{\text{KL}}$  polynomials are linear in the  $\xi_i$ . General expressions for  $\Psi_i$ , including higher order terms, can be found in [9].

We rely on Eq. (16) to form representations of the stochastic velocity, pressure, and temperature distributions. Governing equations for the unknown expansion coefficients are obtained by inserting the expansion into the governing equations and using a Galerkin approach that takes advantage of the orthogonality of the polynomial chaoses [1, 9]. This results in the coupled system

$$\frac{\partial \mathbf{u}_k}{\partial t} + (\mathbf{u} \cdot \nabla \mathbf{u})_k = -\nabla p_k + \frac{Pr}{\sqrt{Ra}} \nabla^2 \mathbf{u}_k + Pr \theta_k \mathbf{e}_y, \quad (17)$$

$$\nabla \cdot \mathbf{u}_k = 0, \quad (18)$$

$$\frac{\partial \theta_k}{\partial t} + \nabla \cdot (\mathbf{u} \theta)_k = \frac{1}{\sqrt{Ra}} \nabla^2 \theta_k, \quad (19)$$

for  $k = 0, \dots, P$ . Here,  $\mathbf{u}_k(\mathbf{x}, t)$ ,  $p_k(\mathbf{x}, t)$ , and  $\theta_k(\mathbf{x}, t)$  are the coefficients in the PC expansion of the normalized velocity, pressure, and temperature fields, respectively. The quadratic velocity–velocity and velocity–temperature products are given by

$$(\mathbf{u} \cdot \nabla \mathbf{u})_k = \sum_{i=0}^P \sum_{j=0}^P C_{ijk} \mathbf{u}_i \nabla \mathbf{u}_j \quad (20)$$

and

$$(\mathbf{u}\theta)_k = \sum_{i=0}^P \sum_{j=0}^P C_{ijk} \mathbf{u}_i \theta_j, \quad (21)$$

where

$$C_{ijk} \equiv \frac{\langle \Psi_i \Psi_j \Psi_k \rangle}{\langle \Psi_k^2 \rangle}. \quad (22)$$

Note that although  $C_{ijk} = 0$  for  $1 \leq i, j, k \leq N_{\text{KL}}$ , it is generally nonvanishing, so that the Galerkin procedure results in a coupled system for the velocity and temperature modes. Note, however, that the velocity divergence constraints are decoupled, which enables us to adapt the SPM developed in [1]. This approach is outlined in the following sections.

#### 4.1. Boundary Conditions

Following [1], boundary conditions are treated in a “weak sense”; i.e., the Galerkin approach is also applied at the boundaries. In particular, the PC decomposition is also introduced into the corresponding expressions, and orthogonal projections are used to derive boundary conditions for the velocity and temperature modes. For the setup outlined in Section 3, we obtain

$$\mathbf{u}_k = 0, \quad k = 0, \dots, P \quad \forall \mathbf{x} \in \partial\Omega, \quad (23)$$

$$\frac{\partial \theta_k}{\partial y} = 0, \quad k = 0, \dots, P \quad \text{for } y = 0 \text{ and } y = 1, \quad (24)$$

$$\theta_0(x = 0, y) = \frac{1}{2}, \quad \theta_0(x = 1, y) = -\frac{1}{2}, \quad (25)$$

$$\theta_k(x = 0, y) = 0, \quad \theta_k(x = 1, y) = \sqrt{\lambda_k} f_k(y) \quad \text{for } k = 1, \dots, N_{\text{KL}}, \quad (26)$$

$$\theta_k(x = 0, y) = \theta_k(x = 1, y) = 0 \quad \text{for } k > N_{\text{KL}}. \quad (27)$$

Here  $\Omega = [0, 1] \times [0, 1]$  denotes the computational domain, and  $\partial\Omega$  is its boundary.

#### 4.2. Solution Method

As mentioned earlier, the solution scheme is an adapted version of the SPM introduced in [1]. Numerical integration of the governing equations of the stochastic mode follows an explicit fractional step procedure that is based on first advancing the velocity and temperature modes using

$$\tilde{\mathbf{u}}_k = \frac{4\mathbf{u}_k^n - \mathbf{u}_k^{n-1}}{3} + \frac{2\Delta t}{3} \left[ -2(\mathbf{u} \cdot \nabla \mathbf{u})_k^n + (\mathbf{u} \cdot \nabla \mathbf{u})_k^{n-1} + \frac{Pr}{\sqrt{Ra}} \nabla^2 \mathbf{u}_k^n + Pr \theta_k^n \mathbf{e}_y \right], \quad (28)$$

$$\theta_k^{n+1} = \frac{4\theta_k^n - \theta_k^{n-1}}{3} + \frac{2\Delta t}{3} \left[ \nabla \cdot (-2(\mathbf{u}\theta)_k^n + (\mathbf{u}\theta)_k^{n-1}) + \frac{1}{\sqrt{Ra}} \nabla^2 \theta_k^n \right], \quad (29)$$

where superscripts refer to the time level and  $\Delta t$  is the time step. Note that since we are primarily interested in the steady-state solution of this system, we have combined explicit second-order time discretization of the convective terms and with first-order discretization of the buoyancy and viscous terms. As in [1], spatial derivatives are approximated using second-order centered differences. In the second fractional step, the “intermediate” velocity modes  $\tilde{\mathbf{u}}_k$  are updated so as to satisfy the divergence constraints [35, 36]; we use

$$\mathbf{u}_k^{n+1} = \tilde{\mathbf{u}}_k - \frac{2\Delta t}{3} \nabla p_k^{n+1}, \quad (30)$$

where  $p_k$  are solutions to the Poisson equations

$$\nabla^2 p_k^{n+1} = \frac{3}{2\Delta t} \nabla \cdot \tilde{\mathbf{u}}_k \quad (31)$$

with homogeneous Neumann conditions [35, 36]. Note that these elliptic systems for the various modes are *decoupled*, a key feature in the efficiency of SPM [1].

In the implementations presented in the following, we relied on a conservative second-order finite-difference discretization on a uniform Cartesian mesh with  $(N_x, N_y)$  cells in the  $x$  and  $y$  directions respectively. A direct, Fourier-based, fast Poisson solver is used to invert Eqs. (31). Since these inversions account for the bulk of the CPU times, and since systems for individual modes are decoupled, the computational cost scales essentially as  $O(N \log N)$ , where  $N \equiv N_x \times N_y \times (P + 1)$ . This estimate is in fact reflected in the tests that follow.

## 5. DETERMINISTIC PREDICTION

We start with a brief discussion of deterministic predictions, obtained by setting the order ( $N_0$ ) of the PC expansion to zero. In this case, the stochastic boundary conditions reduce to those of the classical problem with uniform hot and cold wall temperatures,  $\theta_h = 1/2$  and  $\theta_c = -1/2$ . The resulting predictions are used to validate the computations and to select a

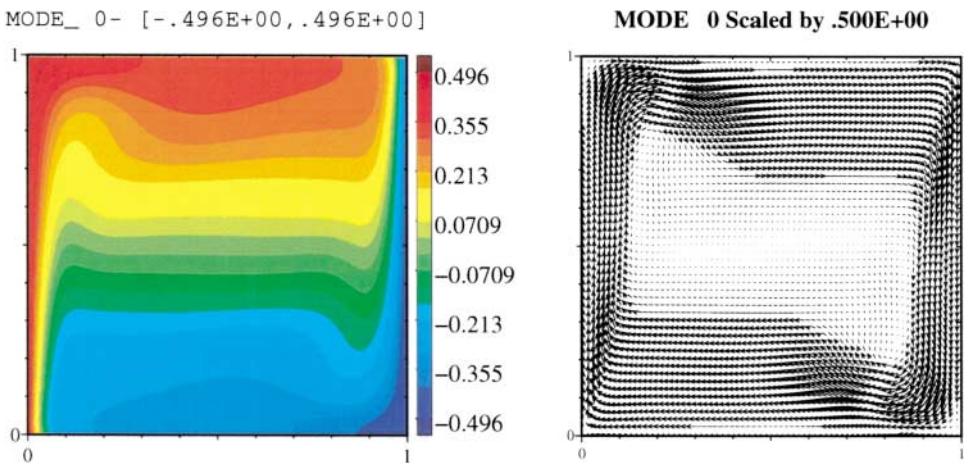


**FIG. 3.** Scaled temperature field (left) and velocity vectors (right) for the deterministic temperature boundary conditions ( $\theta_h = -\theta_c = 1/2$ ) computed using zero-order spectral expansion ( $N_0 = 0$ ).

suitable grid size. To this end, the results are compared with the spectral computations of Le Quéré [12]. For  $Ra = 10^6$ , Le Quéré found a steady Nusselt number  $Nu = 8.8252$ , with the Nusselt number defined by

$$Nu \equiv - \int_0^1 \frac{\partial \theta}{\partial x} dy. \quad (32)$$

Following a systematic grid refinement study, we find that a computational grid with  $N_x = 140$  and  $N_y = 100$  is sufficient for accurate predictions. Starting from an initial state of rest, the computations are carried out until steady conditions are reached. Specifically, the computations are stopped when the maximum change in any field quantity falls below a tolerance  $\epsilon = 10^{-10}$ . (Double precision arithmetic is used.) For the current grid resolution, the steady Nusselt number is found to be  $Nu = 8.8810$ , which is within 0.63% of the prediction of Le Quéré. The structure of the steady field, depicted in Fig. 3, reveals thermal boundary layers on the hot and cold walls and a clockwise circulation of the fluid; these predictions are also in good agreement with the results reported in [12].

## 6. CONVERGENCE ANALYSIS

An analysis of the convergence of the spectral representation scheme is performed in this section. Following the previous discussion, we are presently dealing with a two-parameter discretization that involves the number  $N_{KL}$  of Karhunen–Loève modes, as well as the order  $N_O$  of the PC expansion. As discussed in [9], the total number  $P$  of orthogonal polynomials increases monotonically with  $N_{KL}$  and  $N_O$  [9].

### 6.1. Convergence of KL Expansion

In Section 3, we observed that the KL expansion converged rapidly and consequently speculated that truncation of this expansion would have little effect on the predictions. We now examine this expected trend by computing the mean Nusselt number,

$$\overline{Nu} = - \int_0^1 \frac{\partial \theta_0}{\partial x} dy, \quad (33)$$

and its standard deviation,

$$\sigma(Nu) = \left( \sum_{i=1}^P \left\{ \left[ - \int_0^1 \frac{\partial \theta_i}{\partial x} dy \right]^2 \langle \Psi_i \Psi_i \rangle \right\} \right)^{1/2}, \quad (34)$$

for  $N_{KL}$  ranging from 2 to 10. For brevity, we restrict our attention to a first-order PC expansion, and results are obtained with fixed  $L_c = 1$  and  $\sigma_\theta = 0.25$ .

The average of the local heat flux variance along the wall is given by

$$\overline{\sigma^2(\partial \theta / \partial x)} = \int_0^1 \sum_{i=1}^P \left[ \frac{\partial \theta_i}{\partial x} \right]^2 \langle \Psi_i \Psi_i \rangle dy. \quad (35)$$

and should be carefully distinguished from  $\sigma^2(Nu)$ . At steady state, the net heat flux on the hot wall equals that on the cold wall; since this relationship holds for arbitrary realization,

**TABLE III**  
**Effect of  $N_{\text{KL}}$  on  $\overline{Nu}$  and  $\sigma(Nu)$  for  $N_{\text{O}} = 1$ ,  
 $L_c = 1$ , and  $\sigma_\theta = 0.25$**

$N_{\text{KL}}$	$\overline{Nu}$	$\sigma(Nu)$	$P$
2	8.96344	2.47009	2
4	8.97114	2.46979	4
6	8.97179	2.46980	6
8	8.97190	2.46980	8
10	8.97192	2.46980	10

$\sigma^2(Nu)$  has the same value on the hot wall as on the cold wall. On the other hand,  $\overline{\sigma^2(\partial\theta/\partial x)}$  is expected to assume a higher value on the cold wall, where random fluctuations are imposed, than on the hot wall, since these fluctuations are expected to be smoothed out by diffusion.

Computed values of  $\overline{Nu}$  and  $\sigma(Nu)$  are reported in Table III. As expected, the results show that for the present conditions  $\overline{Nu}$  and  $\sigma(Nu)$  converge rapidly with  $N_{\text{KL}}$ . To further examine the predictions, we plot in Fig. 4 the distribution of the normalized heat flux  $-\partial\theta/\partial x$  along the hot and cold walls as a function of  $P$ . (Note that for  $N_{\text{O}} = 1$ ,  $P = N_{\text{KL}}$ .) Clearly, on the hot wall, only modes 0 and 1 contribute significantly to the local heat flux; for the higher modes,  $\partial\theta_i/\partial x$  is close to zero for all  $y$ . This situation contrasts with the distribution of the heat fluxes on the cold wall, where significant heat flux fluctuations are observed for all the PC modes. However, as noted earlier, the net heat fluxes across the hot and cold walls are equal at steady state. Thus, when integrated along the boundary, the significant fluctuations of the higher modes on the cold wall tend to cancel out. This explains the rapid convergence of integral quantities in Table III.

The standard deviation of the local heat flux, shown in Fig. 5, closely reflects these trends. In particular, by comparing points symmetrically across the midplane, the results clearly show that the values on the cold wall are generally larger than those on the hot wall. Also note that the curve for the cold wall exhibits a noticeable waviness that

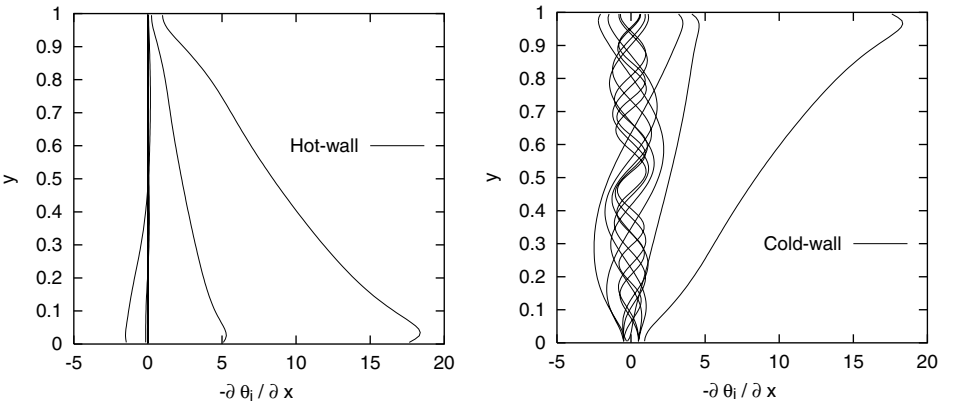


**FIG. 4.** Local heat fluxes versus  $y$  on the hot (left) and cold (right) walls, for modes 0–10. A first-order expansion is used with  $N_{\text{KL}} = 10$ ,  $L_c = 1$ , and  $\sigma_\theta = 0.25$ .

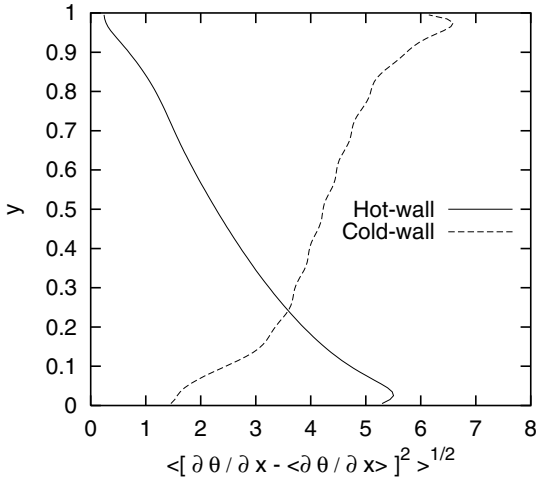


**FIG. 5.** Standard deviation of the local heat fluxes versus  $y$  on the hot and cold walls. A first-order expansion is used with  $N_{\text{KL}} = 10$ ,  $L_c = 1$ , and  $\sigma_\theta = 0.25$ .

corresponds to the imposed conditions, whereas the curve for the hot-wall distribution is smooth.

## 6.2. Convergence of PC Expansion

In this section, we analyze the convergence of the PC expansion by contrasting results obtained with  $N_O = 1, 2$ , and  $3$ . Results are obtained with  $L_c = 1$  and  $\sigma_\theta = 0.25$ , using both four and six KL modes.

*Wall heat transfer.* The computed values of  $\overline{Nu}$  and  $\sigma(Nu)$  are reported in Table IV, together with the number  $P$  of polynomials used. The results exhibit a fast convergence as the order of the PC expansion,  $N_O$ , increases. The differences in  $\overline{Nu}$  and  $\sigma(Nu)$  between second- and third-order solutions are less than 0.01% and 0.05%, respectively. The close quantitative agreement between the results for  $N_O = 2$  and  $3$  indicates that, at least as far as integral quantities are concerned, a second-order expansion is sufficiently accurate. This fast convergence rate is also indicative of the smooth dependence of the solution with respect to the imposed random temperature fluctuations.

Plotted in Fig. 6 are the heat flux distributions along the cold (top row) and hot (bottom row) walls for  $N_O = 1, 2$ , and  $3$ . Results are obtained with  $N_{\text{KL}} = 4$  and curves are plotted

**TABLE IV**

**Mean Nusselt Number and Its Standard Deviation for First-, Second-, and Third-Order PC Expansion with  $N_{\text{KL}} = 4$  and  $6$  for  $L_c = 1$  and  $\sigma_\theta = 0.25$**

$N_O$	$\overline{Nu}$		$\sigma(Nu)$		$P$	
	$N_{\text{KL}} = 4$	$N_{\text{KL}} = 6$	$N_{\text{KL}} = 4$	$N_{\text{KL}} = 6$	$N_{\text{KL}} = 4$	$N_{\text{KL}} = 6$
1	8.97114	8.97179	2.46979	2.46980	5	7
2	8.97289	8.97352	2.46323	2.46327	15	27
3	8.97337	8.97340	2.46239	2.46245	34	83

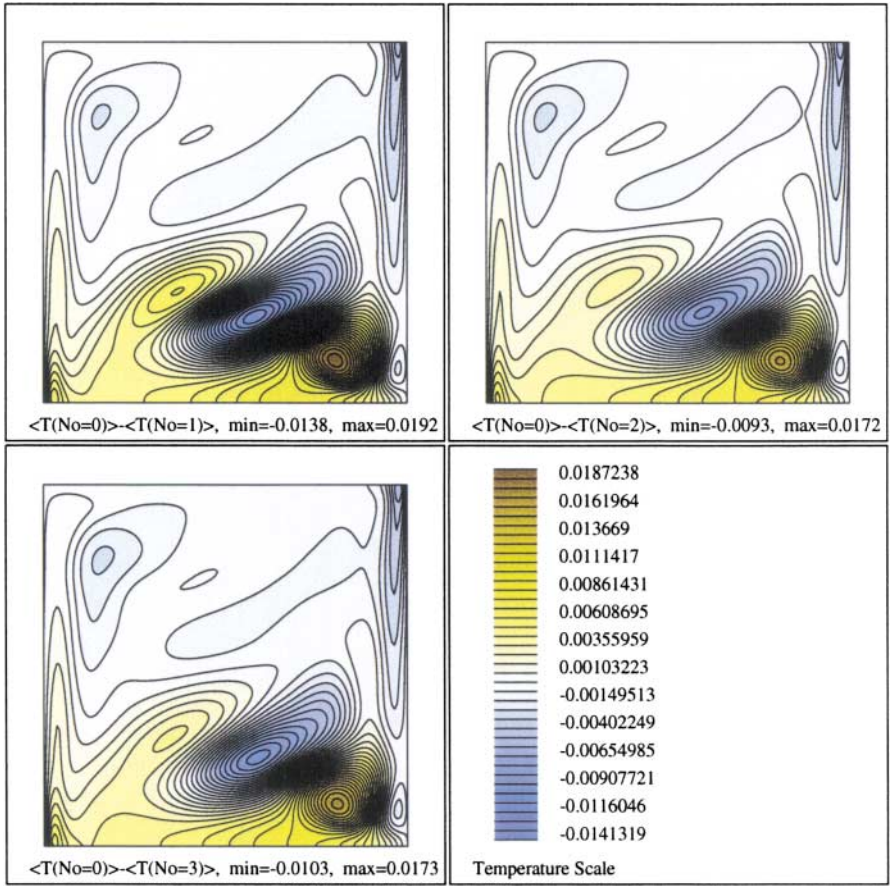


**FIG. 8.** Contours of  $\theta^0 - \langle \theta^{N_0} \rangle$ . Plots are generated for  $N_0 = 1, 2$ , and  $3$ . Results are obtained with  $N_{\text{KL}} = 4$ ,  $L_c = 1$ , and  $\sigma_\theta = 0.25$ .

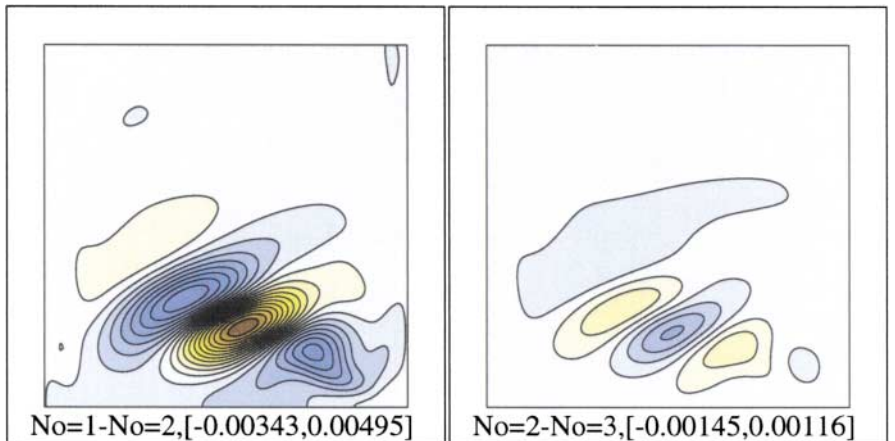


**FIG. 9.** Contour plots of  $\theta^1 - \theta^2$  (left) and  $\theta^2 - \theta^3$  (right). Results are obtained with  $N_{\text{KL}} = 4$ ,  $L_c = 1$ , and  $\sigma_\theta = 0.25$ .

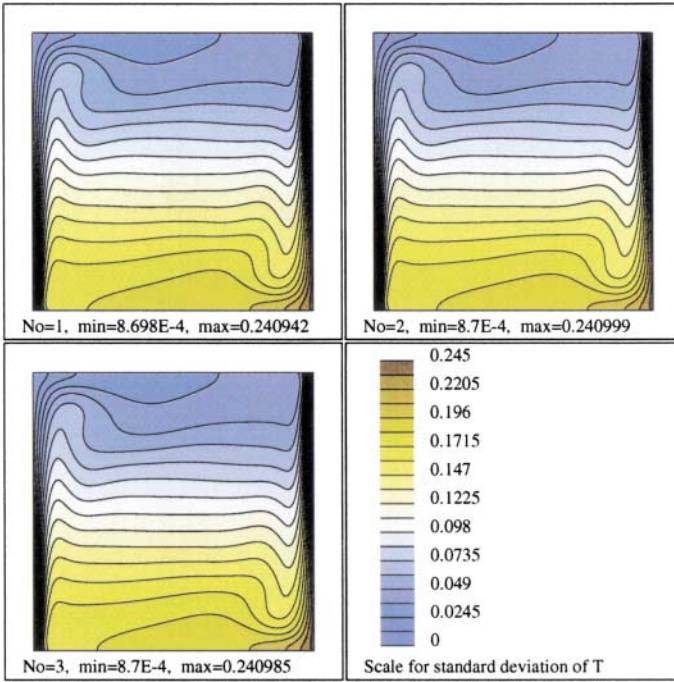


**FIG. 10.** Contours of standard deviation in temperature for  $N_0 = 1, 2$ , and  $3$ . Results are obtained with  $N_{KL} = 4$ ,  $L_c = 1$ , and  $\sigma_\theta = 0.25$ .

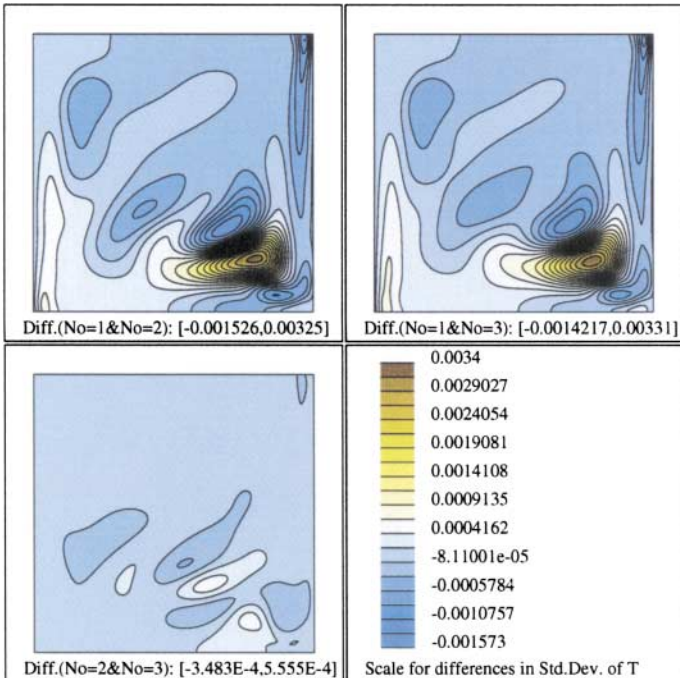


**FIG. 11.** Differences in the temperature standard deviation computed using  $N_0 = 1, 2$ , and  $3$ . In all cases,  $N_{KL} = 6$ ,  $L_c = 1$ , and  $\sigma_\theta = 0.25$ .

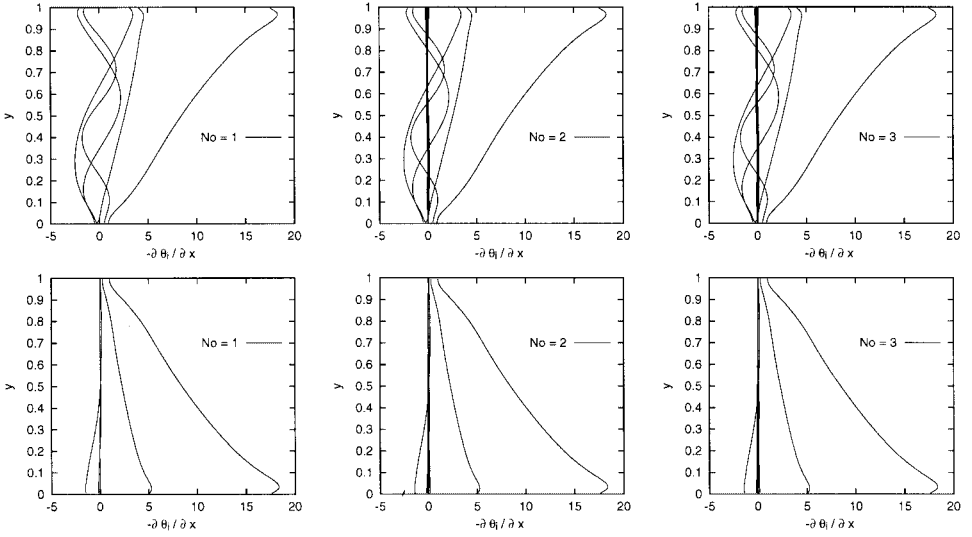


**FIG. 6.** Local heat flux versus  $y$  on the cold (top row) and hot (bottom row) walls. Results are obtained with  $N_{KL} = 4$ ,  $L_c = 1$ , and  $\sigma_\theta = 0.25$ . Curves are plotted for every mode in the PC expansion.  $P = 4$  for  $N_O = 1$ ,  $P = 14$  for  $N_O = 2$ , and  $P = 34$  for  $N_O = 3$ .

for every mode in the PC expansion. The local heat flux profiles for the “first-order modes” (index  $i \leq 4$ ) have shapes similar to those reported in Fig. 4: these modes have significant amplitude on the cold wall, whereas modes higher than 2 are much less pronounced on the hot wall. On both walls, the first-order modes are slightly influenced by the order of the PC expansion. Whereas increasing  $N_O$  introduces more modes in the expansion ( $P = 14$  for  $N_O = 2$  and  $P = 33$  for  $N_O = 3$ ), the heat fluxes associated with these higher order modes are very low. Consequently, the “correction” of the local heat fluxes, arising when  $N_O$  is increased, is weak whenever  $N_O > 1$ . This fact is also shown in Fig. 7, where the local heat-flux standard deviations are plotted for  $N_O = 1, 2$ , and 3.

The present analysis of wall heat fluxes only shows how the solution converges, globally or locally, on the vertical boundaries. To further investigate the behavior of the spectral

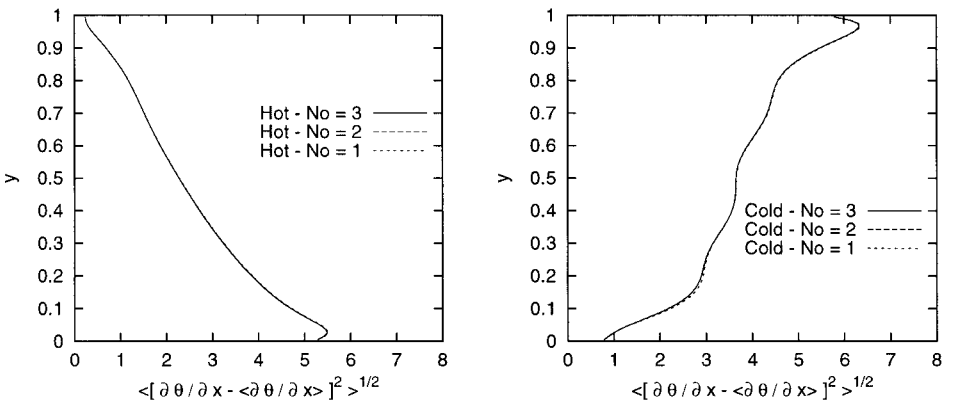


**FIG. 7.** Local standard deviation of the heat fluxes on the hot (left) and cold (right) walls, for  $N_O = 1, 2$ , and 3. Results are obtained with  $N_{KL} = 4$ ,  $L_c = 1$ , and  $\sigma_\theta = 0.25$ .

representation, we analyze the temperature and velocity fields within the cavity. We focus our attention on the distributions of mean quantities and their standard deviations and postpone to Section 7 the examination of individual mode structure.

*Temperature field.* We start by noting that, since the natural convection in the cavity is not a linear process, the mean temperature distribution differs from the deterministic prediction corresponding to the mean temperature boundary condition,  $\theta_c = -1/2$ . This deterministic prediction, corresponding to  $\xi_i = 0$ ,  $i = 1, \dots, N_{\text{KL}}$ , shall be denoted by  $\theta^0$ . Meanwhile, we shall denote by  $\langle \theta^{N_o=1,2,3} \rangle \equiv \theta_0(N_o)$  the mean predictions obtained using first-, second-, and third-order PC expansions, respectively.

Examination of the mean temperature fields obtained with  $N_o = 1, 2$ , and 3 (not shown) reveals that these fields have features like those of  $\theta^0$  (shown earlier in Fig. 3). Thus, we have found it more convenient to analyze the difference fields  $\theta^0 - \langle \theta^{N_o \geq 1} \rangle$ . These difference fields are plotted in Fig. 8 for  $N_{\text{KL}} = 4$ . A close agreement is observed between the plots corresponding to the different expansion orders. Only a very weak dependence of the local magnitudes on  $N_o$  can be detected. Thus, increasing  $N_o$  has only a weak effect on the expected temperature field. To further demonstrate the convergence of the spectral representation, the differences  $\langle \theta^{N_o=1} \rangle - \langle \theta^{N_o=2} \rangle$  and  $\langle \theta^{N_o=2} \rangle - \langle \theta^{N_o=3} \rangle$  are displayed in Fig. 9. The results show that, at least as far as the mean field is concerned, the first-order expansion captures most of the effects of uncertainty. The difference  $\langle \theta^{N_o=2} \rangle - \langle \theta^{N_o=3} \rangle$  is very small, indicating that the truncated terms have a weak impact on the mean temperature.

Figure 8 also shows that the mean temperature along the cold wall is higher than that of  $\theta^0$ . The opposite situation is reported along the hot wall, where the mean temperature is lowered by the uncertainty. These changes are responsible for the improvement of the global heat-transfer coefficient  $\overline{Nu}$ . In addition, the mean temperature on the bottom of the cavity is significantly lower than that of  $\theta^0$ ; in the upper part of the cavity, the mean and deterministic predictions are nearly equal. To explain these trends, one notes that the mean clockwise flow circulation is not altered by the stochastic boundary conditions (as will be shown later). So, on average, the fluid is traveling downward along the cold wall, where it is affected by random temperature conditions. The random fluctuations are transported across the cavity to the hot wall. As the fluid travels upward along the hot wall, uncertainty is reduced due to diffusion, so that when reaching the upper part of the cavity, the fluid temperature has lost most of its uncertainty, and its mean value is close to that of  $\theta^0$ . We also observe that the deviation of the mean temperature field from  $\theta^0$  exhibits a complex structure, with alternating signs, in the lower right quadrant, where the deviation from  $\theta^0$  peaks. This pattern is closely correlated with the uncertainties in the velocity fields, as will be further discussed.

Additional insight into the role of stochastic boundary conditions can be gained from Fig. 10, which depicts the temperature standard deviation fields for  $N_o = 1, 2$ , and 3. The results show that the standard deviation distribution has a structure similar to that of the mean, with two layers parallel to the vertical walls and a horizontal stratified arrangement from the bottom to the top of the cavity. The standard deviation vanishes on the hot wall, where deterministic conditions are imposed, and reaches its maximum on the cold wall, with values close to  $\sigma_\theta$ . This spatial distribution is consistent with the arguments just presented regarding the role of circulation in driving the uncertainty.

Finally, in Fig. 11, it is shown that the expansions for  $N_o = 1, 2$ , and 3 provide essentially the same estimate of the temperature standard deviation, with differences in the fourth

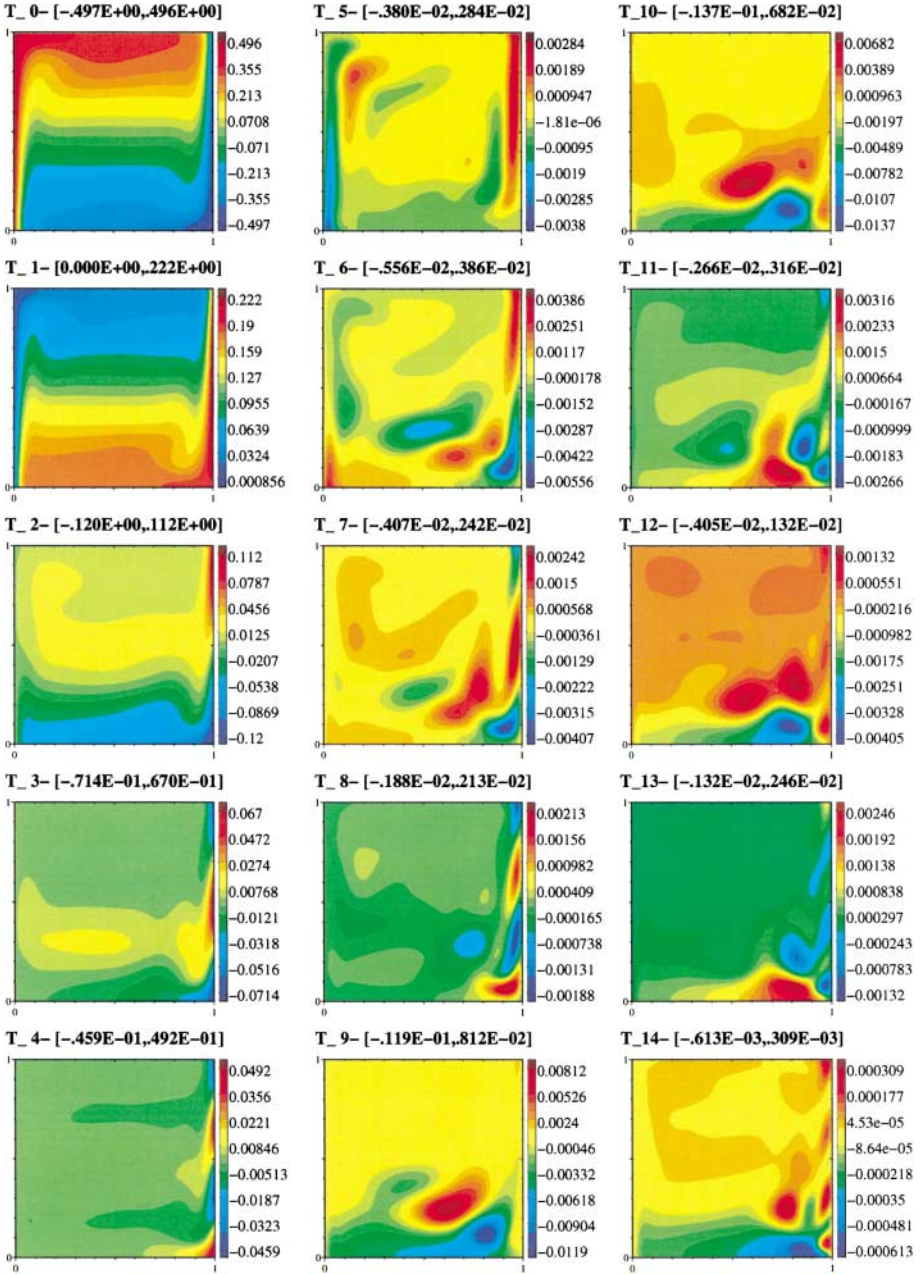


FIG. 17. Scaled temperature fields  $\theta_k$  for  $k = 0, \dots, 14$ . Results are obtained with  $N_{\text{KL}} = 4$ ,  $N_O = 2$ ,  $L_c = 1$ , and  $\sigma_\theta = 0.25$ .

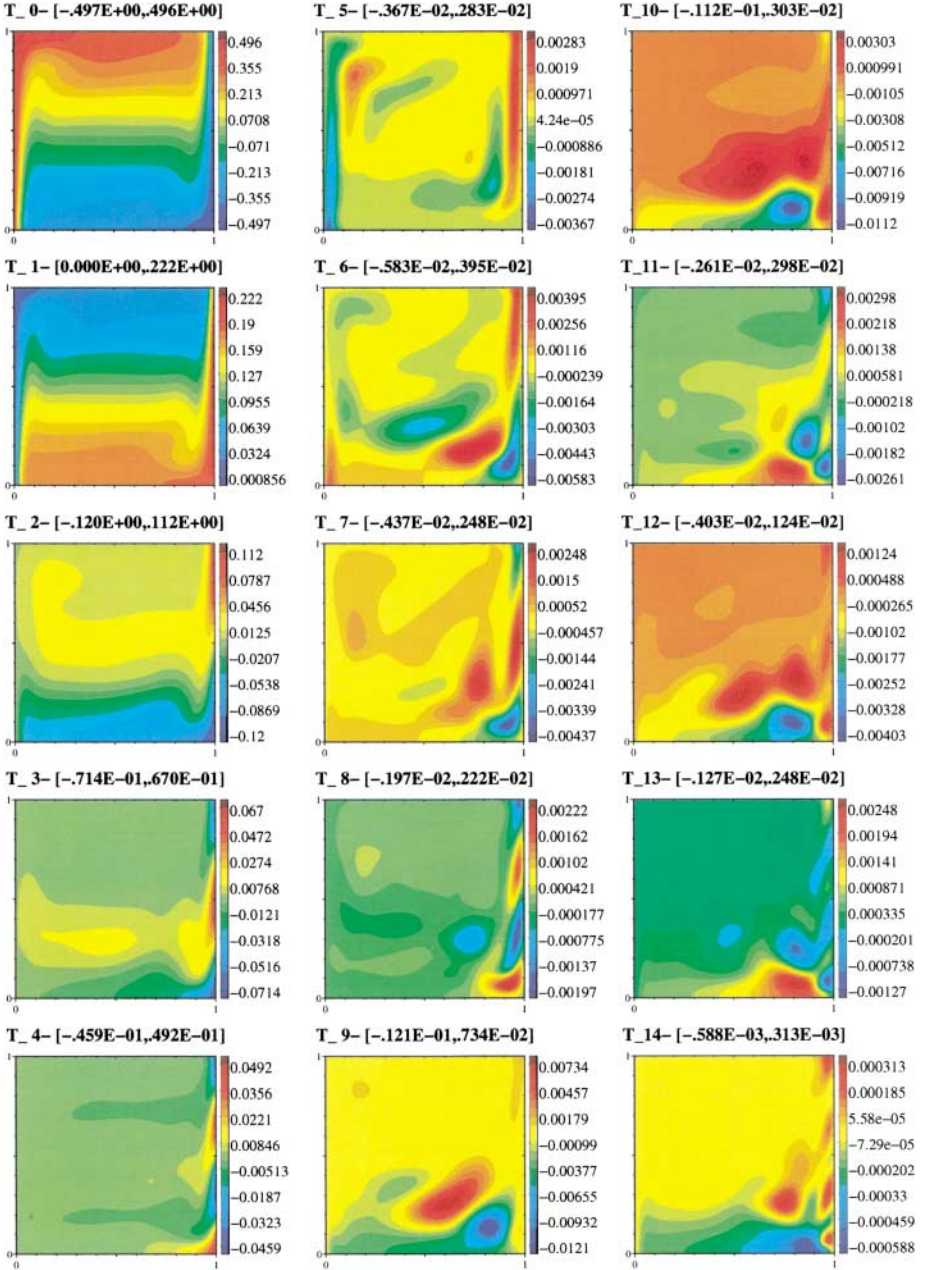
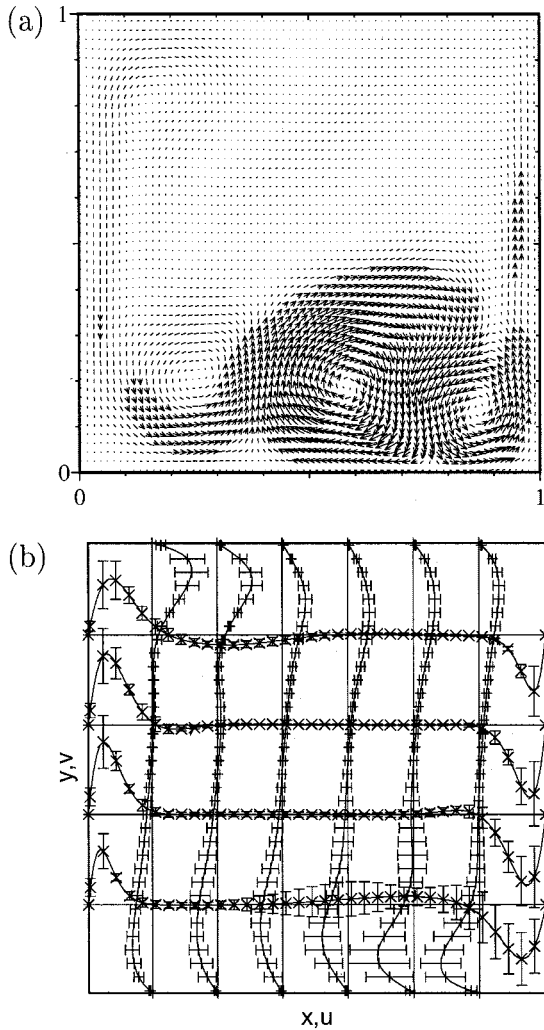


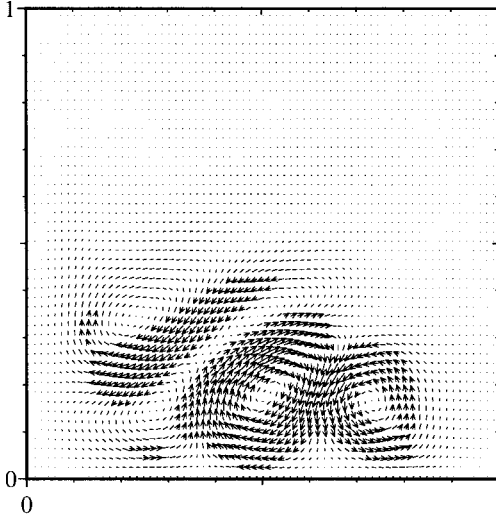
FIG. 19. Scaled temperature fields  $\theta_k$  for  $N_{KL} = 4$ , obtained using NISP/GH predictions with  $N_d = 81$ .  $L_c = 1$ , and  $\sigma_\theta = 0.25$ .

**(No=3)–(No=0)–Scale=5**

**FIG. 12.** (a) Velocity map of the difference  $\langle \mathbf{u}^{N_o=3} \rangle - \mathbf{u}^0$ . (b) Profiles of mean horizontal velocity ( $\langle u^{N_o=3} \rangle$ ) and mean vertical velocity ( $\langle v^{N_o=3} \rangle$ ). The profiles are independently scaled for clarity. The scaled length of the bars corresponds to 6 times the local standard deviation. Results are obtained with  $N_{KL} = 6$ ,  $L_c = 1$ , and  $\sigma_\theta = 0.25$ .

significant digit. These results also demonstrate the fast convergence rate of the spectral expansion and the fact that in the present case a first-order expansion captures most of the standard deviation.

*Velocity field.* As was done for the temperature distribution, we start by examining the deviation of the mean velocity field from  $\mathbf{u}^0$ , which denotes the deterministic solution corresponding to the mean temperature condition ( $\theta_c = -1/2$ ). The mean velocity fields corresponding to first-, second-, and third-order PC expansions will be denoted by  $\langle \mathbf{u}^{N_o=1,2,3} \rangle$ , respectively. For each case, we find that the deviation of the mean solution from  $\mathbf{u}^0$  is small, and we consequently focus on the differences  $\langle \mathbf{u}^{N_o \geq 1} \rangle - \mathbf{u}^0$ .

**(No=3)–(No=2)–Scale=50**

**FIG. 13.** Velocity map of the difference  $\langle \mathbf{u}^{N_0=3} \rangle - \langle \mathbf{u}^{N_0=2} \rangle$ . Results are obtained with  $N_{\text{KL}} = 6$ ,  $L_c = 1$ , and  $\sigma_\theta = 0.25$ .

Figure 12a shows the distribution of  $\langle \mathbf{u}^{N_0=3} \rangle - \mathbf{u}^0$  for a simulation with  $N_{\text{KL}} = 6$ ,  $L_c = 1$ , and  $\sigma_\theta = 0.25$ . The difference field exhibits three complex structures that lie in the lower part of the cavity. While these structures resemble the recirculating eddies of the mean flow, it should be emphasized that the velocity magnitudes have been scaled by a factor of 10 compared to those in Fig. 3. Thus, with respect to  $\mathbf{u}^0$ , the mean field is significantly perturbed in the regions occupied by these structures, but it is not actually recirculating. This can be verified by inspecting the mean solution itself, depicted in Fig. 12b, using the profiles of mean horizontal and mean vertical velocity. The profiles show that the mean flow is not recirculating but that flow “reversal,” hence recirculation, in the lower right corner is likely to occur. In this region, one observes large standard deviations and low mean velocities, especially outside the boundary layers; this is indicative of large sensitivity to the stochastic boundary conditions. This trend is consistent with earlier observations regarding the deviations  $\theta^0 - \langle \theta^{N_0 \geq 1} \rangle$ , which exhibited maxima at these same locations.

To verify that the behavior of the stochastic solution is well represented, and consequently that the previously mentioned trends are not an artifact of the method, we inspect in Fig. 13 the distribution of  $\langle \mathbf{u}^{N_0=3} \rangle - \langle \mathbf{u}^{N_0=2} \rangle$ . The velocity map is generated with a scaling factor that is 10 times larger than that used in Fig. 12a. The results clearly demonstrate that there are very small differences between the second- and third-order solutions and that both provide accurate representations of the stochastic process.

*Remarks.* We close this section with two remarks regarding the ability of the spectral representation to accurately reproduce individual events and regarding the CPU costs of the spectral solution scheme.

Recall that the spectral representation relies on a weighted residual procedure to determine the mode coefficients. This representation is the closest polynomial to the exact

## Scale=5

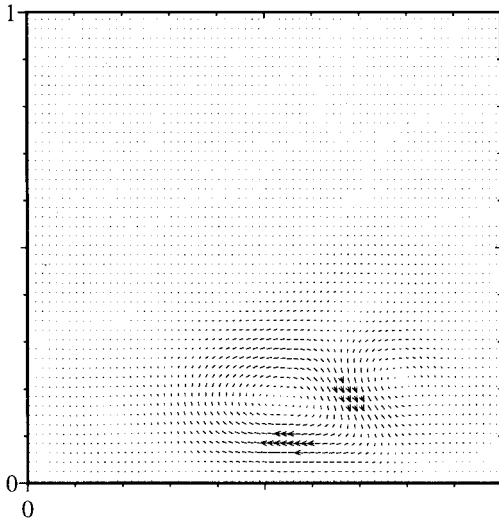


**FIG. 14.** Velocity map of the difference  $\mathbf{u}^{N_0=2}(\boldsymbol{\xi} = 0) - \mathbf{u}^0$ . Results are obtained with  $N_{\text{KL}} = 6$ ,  $L_c = 1$ , and  $\sigma_\theta = 0.25$ .

response “surface” in the corresponding  $L_2$  norm. Although optimal in this sense, the PC representation does not guarantee that individual “realizations” are exactly interpolated. However, our experiences indicate that when the PC representation is of sufficiently high order, it can also be used to obtain highly accurate estimates of individual realizations. This quality is illustrated in Fig. 14, where we plot the difference between  $\mathbf{u}^0$  and the second-order solution evaluated at  $\boldsymbol{\xi} = 0$ , i.e.,  $\mathbf{u}^{N_0=2}(\boldsymbol{\xi} = 0)$ . The figure is generated with a scaling factor 10 times larger than that used for the deterministic solution of Fig. 3, demonstrating that the agreement between  $\mathbf{u}^0$  and  $\mathbf{u}^{N_0=2}(\boldsymbol{\xi} = 0)$  is indeed very good.

Regarding the performance of the spectral computations, we had anticipated earlier that the CPU cost would scale linearly with  $P$ , with near unity coefficient. As shown in Fig. 15, this behavior is in fact observed, and, together the spectral behavior of the errors in the spectral approximation, can be used to guide the selection of a suitable stochastic discretization level that properly balances accuracy and CPU cost.

## 7. MODE BEHAVIOR

In this section, we examine individual velocity and temperature modes in PC expansion. For brevity, we restrict our attention to spectral predictions obtained with  $N_{\text{KL}} = 4$ ,  $N_0 = 2$ ,  $L_c = 1$ , and  $\sigma_\theta = 0.25$ . For this spectral resolution  $P = 14$ , giving a total of 15 modes. Thus, we end up with a moderate number of velocity and temperature distributions, which are analyzed in the following.

### 7.1. Velocity

Figure 16 provides vector maps for all the modes in the computations. Different scaling factors are used to represent the various fields, as indicated in the labels. Note that the zeroth

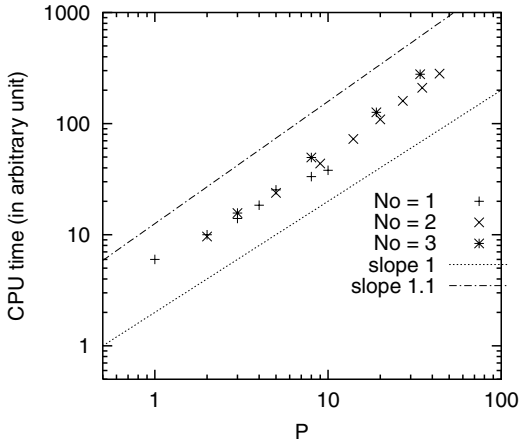


**FIG. 15.** CPU time needed to perform 100 time steps for PC expansions with different  $N_O$  and  $N_{KL}$ . A fixed mesh size of  $140 \times 100$  cells is used. Scaled CPU times are reported as a function of the largest polynomial index  $P$ .

mode corresponds to the mean velocity field, which has been already studied in Section 6.2. Thus, we shall focus on the higher modes.

The first-order velocity modes  $v_k$ ,  $k = 1, \dots, 4$ , follow mode 0 in the first column of Fig. 16. They correspond to the polynomial  $\Psi_k = \xi_k$  for  $k = 1, \dots, N_{KL} = 4$ . Thus, these modes reflect the linear response of the stochastic velocity field to the corresponding Karhunen–Loève eigenfunctions appearing in Eq. (13) and plotted in Fig. 1. Note that the first KL mode has a nearly uniform, positive value and that it exhibits a positive velocity along the cold wall and a negative velocity along the hot wall. This is not surprising since, for  $\xi_1 > 0$ , the first Karhunen–Loève mode tends to decrease the temperature difference between the two walls. However, the structure of  $\mathbf{u}_1$  is not similar to that of  $\mathbf{u}_0$ . The two fields are governed by different dynamics, as shown in the Appendix, where the governing equations are given for a first-order PC expansion. One observes that the first mode is advected (and “stretched”) by the mean velocity ( $\mathbf{u}_0$ ) and not by  $\mathbf{u}_1$ . This observation, which also applies for  $\mathbf{u}_2$ ,  $\mathbf{u}_3$ , and  $\mathbf{u}_4$ , remains true for a second-order expansion.

In the neighborhood of the cold wall, all the first-order velocity modes clearly reflect the shape of the corresponding Karhunen–Loève mode. For instance, for  $\mathbf{u}_2$ , the velocity points upward on the highest part of the cold wall and downward in its lowest part, as the associated temperature perturbation is respectively positive and negative (Fig. 1). For  $\mathbf{u}_1$  and  $\mathbf{u}_2$ , the velocity magnitudes are significant near all solid boundaries; on the other hand, for  $\mathbf{u}_3$  and  $\mathbf{u}_4$ , the velocity magnitudes are negligible on the hot wall. For the first-order modes, the velocity magnitudes decrease with increasing mode index; note in particular that the scale factor for  $\mathbf{u}_4$  is twice that of  $\mathbf{u}_3$ . If a larger value for  $N_{KL}$  is used, the additional first-order velocity fields are weaker than those retained, being localized near the cold boundary (not shown). This trend is consistent with our earlier discussion of the weakening effects of the higher frequency, random fluctuations.

The second-order velocity fields  $\mathbf{u}_k$ ,  $k = 5, \dots, 14$ , are plotted in the center and right columns of Fig. 16; the same scaling factor is used for these modes, allowing straightforward comparison. Note that this scaling factor is 80 times larger than that of  $\mathbf{u}_0$  and 10 times

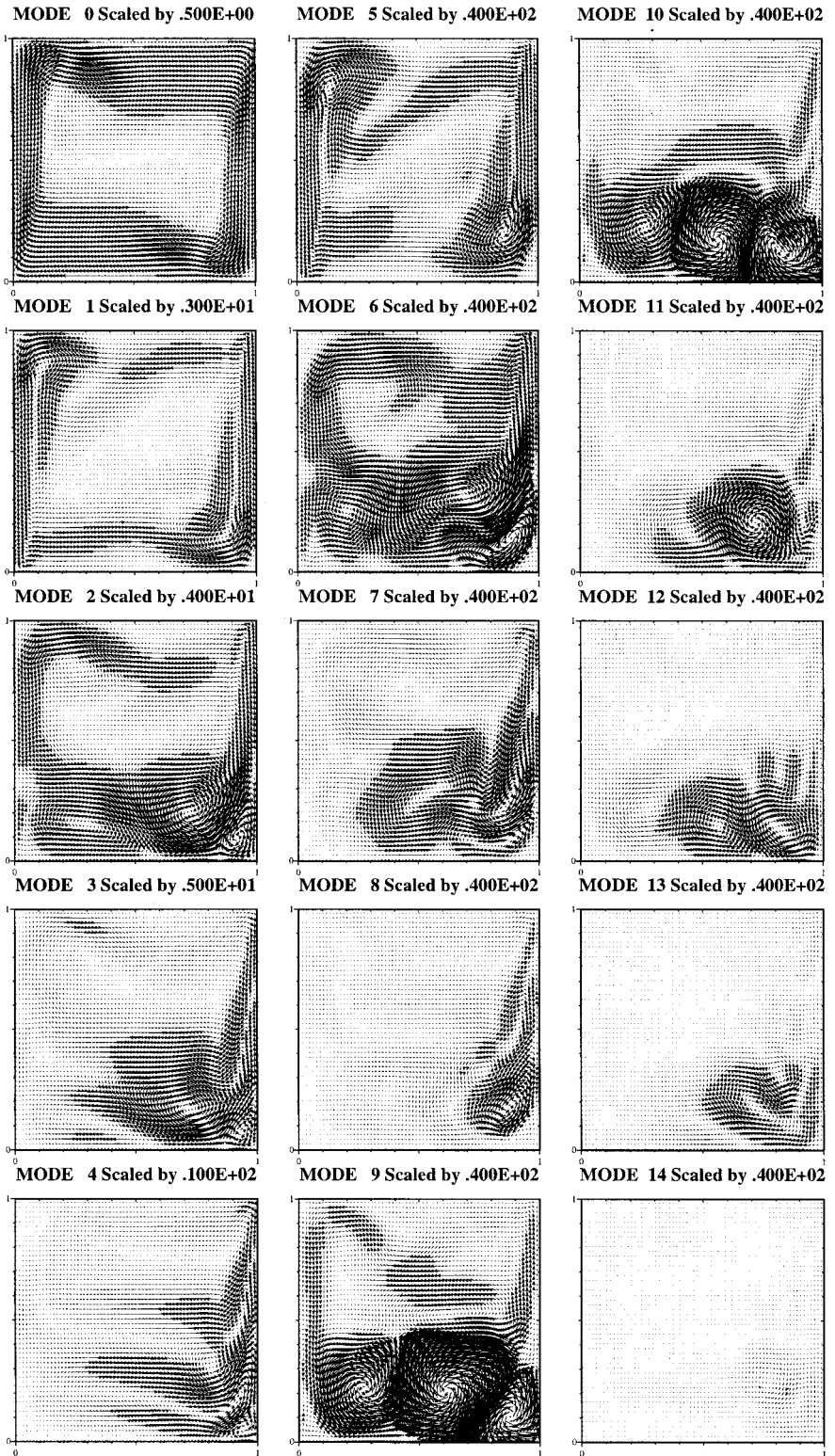


**FIG. 16.** Velocity fields  $u_k$  for  $k = 0, \dots, 14$ . Results are obtained with  $N_{\text{KL}} = 4$ ,  $N_{\text{O}} = 2$ ,  $L_c = 1$ , and  $\sigma_\theta = 0.25$ . Note that different velocity scales are used, as indicated in the labels.

larger than that of  $\mathbf{u}_4$ . Thus, the magnitudes of the second-order velocity fields are much smaller than those of zeroth- and first-order modes. This rapid decay also reflects the rapid convergence of the PC expansion.

The second-order velocity modes have very different patterns, some being only significant along the cold wall and others affecting the entire cavity. Some of these structures can be easily interpreted. For example,  $\mathbf{u}_5$ , which corresponds to  $\Psi_5 = \xi_1^2 - 1$ , has a structure similar to that of  $\mathbf{u}_1$ . For other modes, the structure of the corresponding velocity fields are quite complex and difficult to interpret. It is interesting to note, however, that the velocity fields involving the second KL mode ( $\mathbf{u}_6, \mathbf{u}_9, \mathbf{u}_{10}$ , and  $\mathbf{u}_{11}$ ) seem to have the most significant magnitudes, suggesting that this mode has greater impact on the stochastic process than the others. On the other hand, second-order polynomials associated with the fourth KL mode appear to be very weak.

## 7.2. Temperature

Figure 17 shows contour plots of the temperature modes  $\theta_k, k = 0, \dots, 14$ . Since the mean temperature field  $\theta_0$  has been analyzed earlier, we will focus on first- and second-order modes.

The contours of the first mode,  $\theta_1$ , are similar to those of  $\theta_0$ , even though the corresponding values differ. This is not surprising since these two modes obey similar boundary conditions, with  $\theta_0$  being subjected to a uniform Dirichlet condition on the cold wall, while  $\theta_1$  is nearly uniform there. However, some differences between the distributions of  $\theta_1$  and  $\theta_0$  can be observed at the lower right corner of the cavity. These differences appear to be governed by the circulation of the mean flow in the cavity. To appreciate this effect, we note that it is the mean field  $\mathbf{u}_0$  which contributes to the transport of  $\theta_1$ ; the heat flux associated with  $\mathbf{u}_1$ , which points upward near the cold wall, is dependent on the mean temperature field  $\theta_0$  (see the Appendix). The role of the mean field in the transport of  $\theta_2, \theta_3$ , and  $\theta_4$  can also be appreciated from the corresponding contour plots. Note that  $\theta_2, \theta_3$ , and  $\theta_4$  are very small in the upper half of the cavity but have significant values in the lower part of the cavity and/or in the vicinity of the cold wall. In particular, for  $\theta_3$  and  $\theta_4$  one observes fluctuations of alternating sign that are localized near the cold boundary and that coincide with the shape of the corresponding KL mode.

As for velocity, the second-order temperature modes are more difficult to interpret than the first-order modes. The only structures that can be easily identified are the imposed cold-wall distributions. The results indicate that significant mode coupling occurs, which can be detected by inspecting the modes involving mixed products of the  $\xi_i$ 's. For instance, for  $\theta_7$  a second-order coupling between  $\xi_1$  and  $\xi_3$  is involved; this mode exhibits three distinct zones along the cold wall, which reflect the shape of the third mode in the KL expansion. Apart from such identifiable features, the second-order modes can have complex distributions, some of which are localized in the lower part of the cavity, while others extend throughout the domain.

Regarding the amplitude of the second-order modes, we note those modes involving  $\xi_2$  and  $\xi_3$ , i.e., the second and third KL eigenfunctions, are dominant. Thus, not all second-order modes contribute equally to the stochastic process. In general, however, the second-order temperature modes are at least one order of magnitude lower than the first-order modes. This is consistent with earlier observations regarding the convergence of the expansion.

## 8. NONINTRUSIVE SPECTRAL PROJECTION

To verify the spectral computations of the previous section, a NISP approach is developed. The starting point in NISP is the observation that the modes  $\mathbf{u}_i$  and  $T_i$  can be obtained by projecting deterministic computations onto the PC basis. If  $\mathbf{u}^d(\boldsymbol{\xi})$  and  $T^d(\boldsymbol{\xi})$  denote the deterministic solution corresponding to a particular realization  $\boldsymbol{\xi} = (\xi_1, \dots, \xi_{N_{\text{KL}}})$ , then the polynomial coefficients are, by definition, given by

$$(\mathbf{u}_i, T_i) = \frac{\langle (\mathbf{u}, T)^d \Psi_i \rangle}{\langle \Psi_i \Psi_i \rangle} \equiv \int_{-\infty}^{\infty} d\xi_1 \cdots \int_{-\infty}^{\infty} d\xi_{N_{\text{KL}}} \left[ (\mathbf{u}, T)^d(\boldsymbol{\xi}) \frac{\Psi_i(\boldsymbol{\xi})}{\langle \Psi_i^2 \rangle} \prod_{k=1}^{N_{\text{KL}}} \frac{\exp(-\xi_k^2/2)}{\sqrt{2\pi}} \right]. \quad (36)$$

### 8.1. Gauss–Hermite Quadrature

For moderate values of  $N_{\text{KL}}$ , our multidimensional integration can be efficiently performed using Gauss–Hermite quadrature [30, 31]. Using  $n$  collocation points along each “stochastic direction,” Eq. (36) can be approximated as

$$(\mathbf{u}_i, T_i) = \sum_{n_1=1}^n \cdots \sum_{n_{N_{\text{KL}}}=1}^n (\mathbf{u}, T)^d(x_{n_1}, \dots, x_{n_{N_{\text{KL}}}}) \frac{\Psi_i(x_{n_1}, \dots, x_{n_{N_{\text{KL}}}})}{\langle \Psi_i \Psi_i \rangle} \prod_{k=1}^{N_{\text{KL}}} w_{n_k}, \quad (37)$$

where  $(x_k, w_k)$ ,  $k = 1, \dots, n$ , denote the one-dimensional GH integration points and weights. The quadrature in (37) is exact when the integrand is a polynomial of degree of  $2n - 1$  or less. Thus, the coefficients can be exactly estimated if the process is spanned by polynomials of degree less than or equal to  $(2n - 1)/2$ . In this situation, the number of deterministic realizations  $N_d$  required in the NISP approach for given  $N_{\text{KL}}$  and  $N_O$  is  $N_d = (2N_O - 1)^{N_{\text{KL}}}$ . It should be emphasized that for arbitrary  $N_{\text{KL}}$  and  $N_O$ ,  $N_d$  is always greater than  $P$ , the number of polynomials in the spectral approach used here. Since the CPU time in the spectral approach is approximately  $P$  times that of a deterministic solution, NISP is not as efficient as the spectral approach. Its main advantage, however, is that it makes use of a deterministic solver without the need for any modifications and so is “nonintrusive.”

NISP/GH computations are performed for a case with  $N_{\text{KL}} = 4$  and  $N_O = 2$ . We use  $n = 3$  and so obtain  $N_d = 81$  deterministic realizations for the corresponding GH quadrature points. (In contrast, the intrusive spectral approach discussed previously has  $P = 14$ , for a total of 15 modes.) Velocity and temperature modes obtained using NISP are plotted in Figs. 18 and 19, respectively. The corresponding results obtained using the intrusive spectral approach were given in Figs. 16 and 17 and have extensively discussed in the previous section.

For the velocity fields, we find an excellent agreement between the intrusive spectral results (Fig. 16) and the NISP predictions (Fig. 18) for the zeroth- and first-order modes. For the second-order modes ( $\mathbf{u}_k$ ,  $k = 5, \dots, 14$ ), small deviations are observed between the two sets, but the primary structure of the modes is quite similar. These small deviations are pronounced for coupled modes involving  $\xi_2$  and  $\xi_3$ ; the deviations are substantially smaller for the nonmixed quadratic modes. Despite these small deviations, the agreement between the intrusive and NISP/GH predictions is very satisfactory.

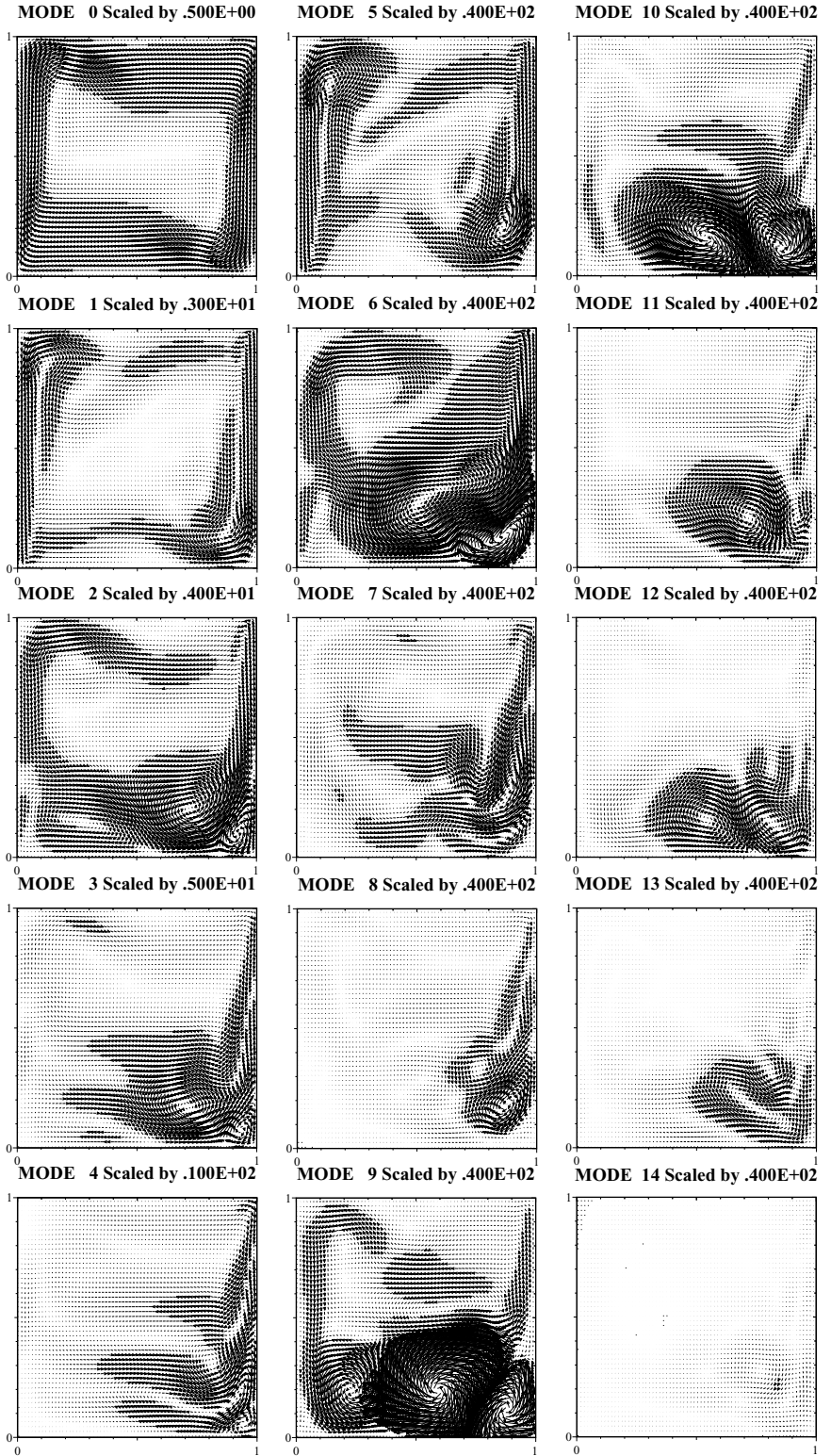


**FIG. 18.** Velocity fields  $\mathbf{u}_i$  for  $N_{\text{KL}} = 4$ , obtained using NISP/GH predictions with  $N_d = 81$ . Note that different scale factors apply on vector magnitudes.  $L_c = 1$  and  $\sigma_\theta = 0.25$ .

Comparison of the temperature modes in Figs. 19 and 17 reveal trends similar to those of the velocity modes. In particular, the zeroth- and first-order modes are in excellent quantitative agreement, as can be appreciated by inspecting the maxima and minima reported on individual frames. These values also provide a good illustration of the deviations observed in the second-order modes. Again the largest differences are observed for modes involving mixed products. The small magnitude of these differences, compared to the characteristic values of the first-order terms, is evident and should be emphasized.

The origin of deviations between intrusive and NISP/GH predictions can be traced to the errors inherent in both approaches. These primarily consist of spectral truncation errors in the intrusive approach and aliasing errors in the NISP predictions. Obviously, complete agreement between NISP and spectral computations can only be achieved in the case of a finite spectrum. Since we are presently dealing with second-order spectral representations, agreement would occur if the third- and higher order modes vanish identically, which is clearly not the case: the third-order terms are very small, but not identically vanishing.

To further examine these differences, we rely on the  $L_2$  norms of the differences between the same temperature modes in two different solutions,  $T^{(1)}$  and  $T^{(2)}$ , defined according to

$$\mathcal{E}_{ik}^2 \equiv \left[ \iint (T_i^{(1)} - T_k^{(2)})^2 dx dy \right]^{1/2}. \quad (38)$$

The indices  $i$  and  $k$  are selected so that  $\Psi_i$  in the PC expansion of  $T^{(1)}$  refers to the same polynomial  $\Psi_k$  in the polynomial expansion for  $T^{(2)}$ . Obviously,  $i = k$  when  $T^{(1)}$  and  $T^{(2)}$  have the same number of KL modes,  $N_{\text{KL}}$ .

We have first compared modal solutions obtained with intrusive spectral computations using the same order PC expansion but different number of KL modes. In this case, the error measure is only relevant for the modes that are shared in both representations, namely, those belonging to the expansion having lower  $N_{\text{KL}}$  value. A sample of this exercise is shown in Fig. 20, which shows the  $L_2$  norm between temperature modes obtained using second-order expansions with  $N_{\text{KL}} = 4$  and 6. As is evident in the figure, the  $L_2$  errors between the

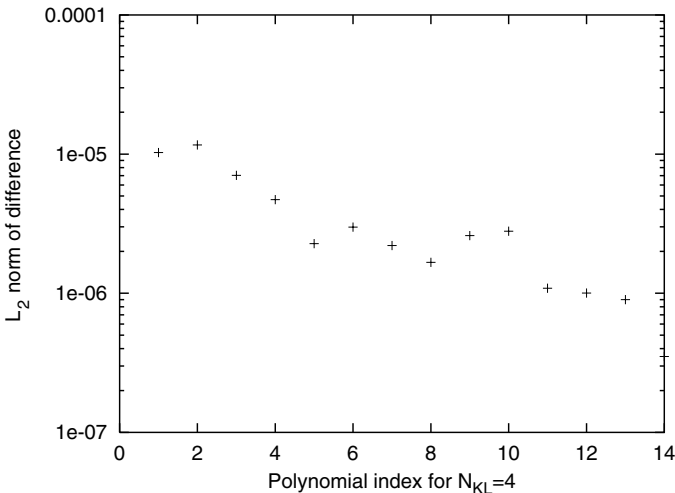


**FIG. 20.**  $L_2$  norm of the difference in the common temperature modes obtained with intrusive spectral calculations using  $N_{\text{KL}} = 4$  and  $N_{\text{KL}} = 6$ . In both cases, a second-order PC expansion is used.

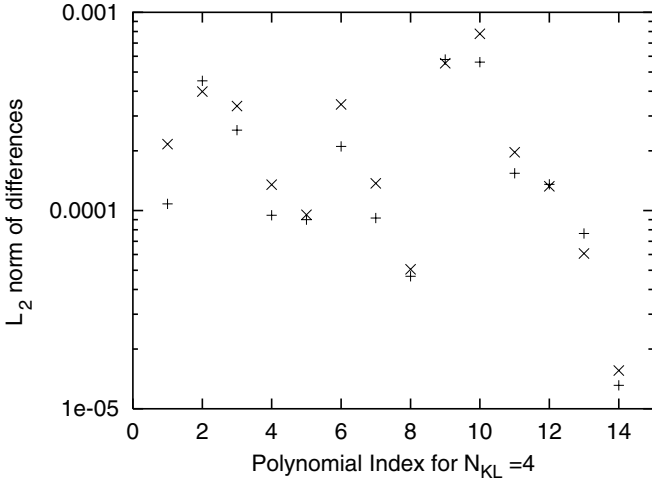


**FIG. 21.**  $L_2$  norms of differences in temperature modes obtained with intrusive spectral predictions using second- and third-order PC expansions (+), and between predictions obtained using the second-order spectral and second-order NISP/GH predictions ( $\times$ ). In all cases,  $N_{\text{KL}} = 4$ .

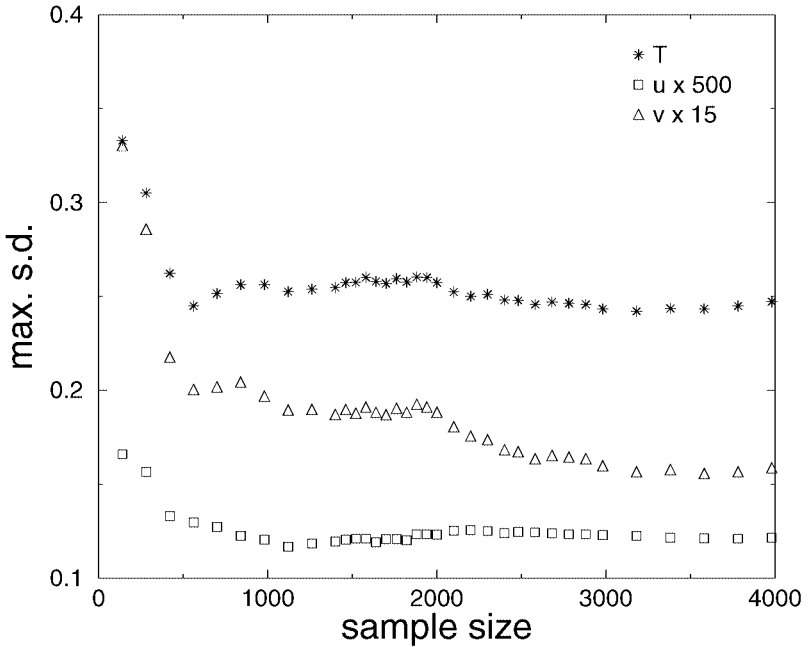
modal solutions are very small, indicating a very good agreement between the predictions. The same analysis was repeated with third-order PC expansions (not shown) and revealed similar trends. This further supports earlier claims that for the present conditions  $N_{\text{KL}} = 4$  is sufficient for adequate representation of the stochastic boundary conditions.

Figure 21 shows the  $L_2$  norm of the differences between the second-order and third-order intrusive predictions and between second-order intrusive and second-order NISP/GH results. In all cases, we use  $N_{\text{KL}} = 4$  and  $L_2$  norms are shown for all 14 modes in the second-order PC expansion. The results indicate that for all modes the  $L_2$  norms are small, with magnitudes falling below  $10^{-3}$ . In addition, the differences between second-order NISP and intrusive predictions are comparable to corresponding deviations obtained using intrusive spectral computations with  $N_{\text{O}} = 2$  and 3. Thus, the deviations between the NISP/GH and intrusive spectral predictions are of the same order as the spectral truncation errors in the latter approach.

## 8.2. Latin Hypercube Sampling

As mentioned earlier, a Latin hypercube sampling approach is also applied to determine PC mode distributions. LHS is a stratified sampling technique where the random variable distributions are divided into equal probability intervals, and events are formed by randomly selecting variables within each of these intervals [32]. LHS typically requires fewer samples than simple pseudo-random sampling to reach the same degree of convergence, and a uniform sampling of phase space is assured within the limits of the sample size. In the computations, the DAKOTA toolkit [37–39] is used to generate the necessary samples of the uncorrelated Gaussian variables appearing in the KL expansion. Individual realizations are then projected onto the PC basis to determine the mode distributions.

NISP/LHS computations are performed for a case with  $N_{\text{KL}} = 6$ ,  $L_c = 1$ , and  $\sigma_\theta = 0.25$ . The sampling tools in DAKOTA were used to generate a six-dimensional array of uncorrelated normalized Gaussians. The convergence of the mode amplitudes and the mean



**FIG. 22.** Maximum standard deviation of temperature,  $u$ -velocity, and  $v$ -velocity over the computational domain plotted vs the sample size. Note that the velocity standard deviations are scaled, as indicated in the legend.

Nusselt number were monitored as the number of realizations increased. An example of the convergence diagnostics is given in Fig. 22, which shows the maximum standard deviation for temperature and velocity in the entire domain as a function of the sample size. For the present set of conditions, a sample of size of 4000 was deemed sufficient for the analysis, even though statistics are evidently not fully converged, as can be appreciated from the figure.

In the following, we discuss results obtained from NISP/LHS computations in light of the aforementioned NISP/GH results and the earlier “intrusive” spectral results. The spatial distributions of PC modes of order  $\leq 2$  obtained using NISP/LHS (not shown) were first compared with corresponding predictions obtained with second- and third-order intrusive computations. The comparison reveals an excellent agreement for the mean and first-order modes but noticeable quantitative and qualitative differences do occur in the second-order modes. We briefly illustrate these differences by plotting in Fig. 23 the  $L_2$  norm of the differences between (i) the NISP/LHS results and the second-order intrusive predictions, and (ii) the NISP/LHS results and third-order intrusive predictions; the  $L_2$  norm of differences between second- and third-order spectral predictions are also shown for comparison. As observed earlier, the second- and third-order predictions are in excellent agreement with each other, with  $L_2$  norms falling below  $10^{-3}$ . The differences between the NISP/LHS and spectral predictions are also small, but the corresponding  $L_2$  norms are about an order of magnitude larger than those of differences between spectral predictions. It can also be observed that the  $L_2$  norms of differences between the NISP/LHS and intrusive predictions are nearly the same for both second-order and third-order spectral expansions. This indicates that the differences between NISP/LHS and spectral results are strongly affected by the sampling errors in the NISP/LHS approach and that, although still small, these errors are substantially larger than spectral truncation errors.

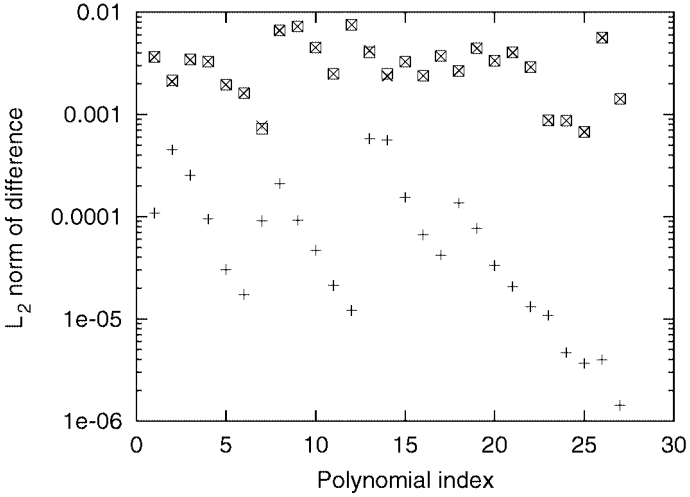


**FIG. 23.**  $L_2$  norm of differences in temperature modes obtained with intrusive spectral predictions using second- and third-order PC expansions (+), intrusive second-order and NISP/LHS with 4000 realizations ( $\times$ ), and intrusive third-order and NISP/LHS with 4000 realizations ( $\square$ ). In all cases,  $N_{\text{KL}} = 6$ , and the comparison is restricted to second-order modes.

Additional insight into the convergence of the NISP/LHS computations can be gained from Fig. 24, which shows the  $L_2$  norm of the differences in mode distributions between the NISP/LHS and second-order intrusive results, as a function of the sample size. Plotted in Fig. 24a are  $L_2$  norms for the mean and first-order modes; results for modes 7–13 are shown in Fig. 24b. Generally, the difference between NISP/LHS and spectral predictions diminishes quickly, but a residual difference remains for all modes as the sample size increases. The difference decays quicker for the mean and the first-order modes (Fig. 24a), than for modes 7–13 (Fig. 24b). As can be observed in Fig. 23, the differences between NISP/LHS and intrusive spectral predictions are such that  $L_2$  norms corresponding to the mean and first-order modes are comparable to or smaller than those corresponding to some of the second-order modes. Since the latter are significantly weaker than the former, this indicates that the NISP/LHS predictions of the higher order modes have large relative errors and are not well converged. This also shows that the sampling errors in NISP/LHS are behind the observed differences in the distributions of second-order modes.

## 9. UNCERTAINTY QUANTIFICATION

We conclude this study with a quantitative analysis of the effects of the stochastic boundary conditions on heat transfer statistics within the cavity. We rely on spectral computations using  $N_{\text{KL}} = 6$ ,  $N_{\text{O}} = 2$ , and a  $140 \times 100$  computational grid. Results are obtained for three different correlation lengths and standard deviations, namely,  $L_c = 0.5, 1, \text{ and } 2$  and  $\sigma_\theta = 0.125, 0.25, \text{ and } 0.5$ .

Computed values of  $\overline{Nu}$  and  $\sigma(Nu)$  are reported in Tables V and VI, respectively. Table V provides the mean Nusselt number along with the difference  $\overline{Nu} - Nu^0$ , where  $Nu^0$  denotes the Nusselt number corresponding to the deterministic prediction with  $\theta_c = -1/2$ . The results show that  $\overline{Nu}$  is larger than  $Nu^0$ . For fixed correlation length,  $\overline{Nu} - Nu^0$  increases

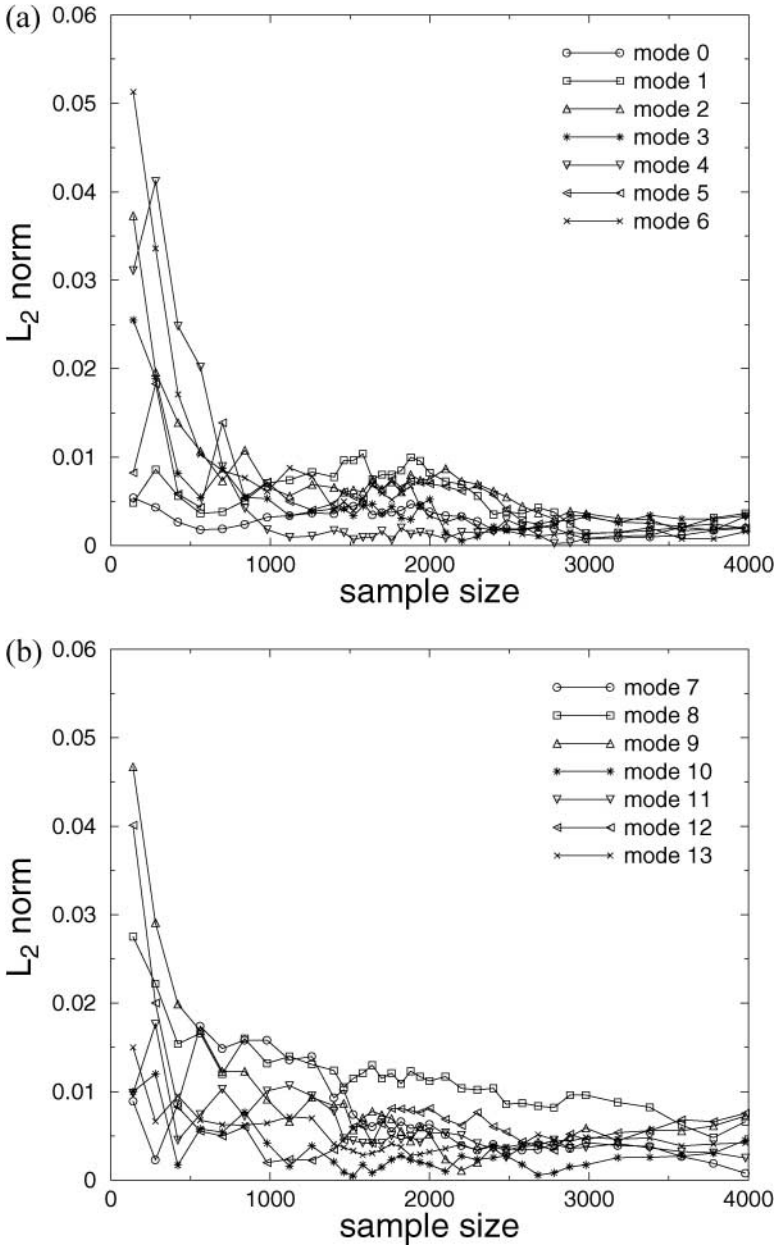


**FIG. 24.**  $L_2$  norm of differences in temperature modes obtained with second-order intrusive and NISP/LHS predictions for different sample size: (a) modes 0–6, (b) modes 7–13. In both approaches,  $N_{\text{KL}} = 6$ ,  $L_c = 1$ , and  $\sigma_\theta = 0.25$ .

approximately as  $\sigma_\theta^2$ . In contrast,  $\overline{Nu}$  exhibits as weaker dependence on  $L_c$ . This is not surprising since, in the range considered, the eigenvalues  $\lambda_i$  of KL modes vary slowly with the correlation length.

Unlike  $\overline{Nu}$ , for fixed  $L_c$  the standard deviation  $\sigma(Nu)$  exhibits an approximately linear dependence on  $\sigma_\theta$ , as in Table VI. Furthermore, compared with the mean,  $\sigma(Nu)$  exhibits a more pronounced dependence on  $L_c$ . This trend is consistent with variations of

**TABLE V**  
**Mean Nusselt Number for Different Values of  $L_c$**   
**and  $\sigma_\theta$  with  $N_{\text{KL}} = 6$  and  $N_O = 2$**

$L_c$	$\sigma_\theta$		
	0.125	0.25	0.5
$\overline{Nu}$			
0.5	8.902	8.967	9.228
1	8.904	8.974	9.268
2	8.905	8.977	9.293
$\overline{Nu} - Nu^0$			
0.5	0.021	0.086	0.347
1	0.023	0.093	0.387
2	0.024	0.096	0.412

the KL mode amplitudes with the correlation length. As  $L_c$  increases, the magnitude of the first KL modes increases, and since these modes have a dominant impact on the uncertainty, so does  $\sigma(Nu)$ .

Figure 25 depicts probability density functions (PDFs) of the Nusselt number computed from the spectral solution. Figure 25a shows that the most likely value of  $Nu$  is not significantly affected by  $\sigma_\theta$ , showing a slight decrease as  $\sigma_\theta$  increases. On the other hand, the skewness of the PDF increases with  $\sigma_\theta$ . In particular, for  $\sigma_\theta = 0.5$ , one observes a flatter tail at high  $Nu$  values than for the lower values. These trends are consistent with earlier results in Table V, which show that  $\overline{Nu} - Nu_0$  increases substantially as  $\sigma_\theta$  increases.

The effect of  $L_c$  on the PDF of the Nusselt number is depicted in Fig. 25b for fixed  $\sigma_\theta = 0.5$ . Consistent with the results of Table VI the PDF becomes wider as  $L_c$  increases. Besides this trend,  $L_c$  appears to have a weak direct influence on the shape of the PDF.

Finally, we note that at  $\sigma_\theta = 0.5$  the PDF can extend into the negative  $Nu$  range. This indicates that in extreme situations, the “mean” temperature on the right vertical wall may exceed the constant value on the left vertical wall, leading to a reversal of the circulation within the cavity and in the wall heat transfer. While such extremes have low probability and consequently make a small contribution to low-order statistics, they demonstrate the capability of the present method of treating situations with large uncertainty. To illustrate these large changes, we plot in Fig. 26 the velocity profiles across the cavity for fixed  $L_c = 1$  and three different standard deviations,  $\sigma_\theta = 0.125, 0.25,$  and  $0.5$ . The length of the “uncertainty” bars is proportional to 6 times the local standard deviation. Clearly, the

**TABLE VI**  
**Standard Deviation of the Nusselt Number for Different**  
**Values of  $L_c$  and  $\sigma_\theta$  with  $N_{\text{KL}} = 6$  and  $N_O = 2$**

$L_c$	$\sigma(Nu)$		
	$\sigma_\theta = 0.125$	$\sigma_\theta = 0.25$	$\sigma_\theta = 0.5$
0.5	1.097	2.186	4.334
1	1.236	2.463	4.859
2	1.322	2.634	5.178

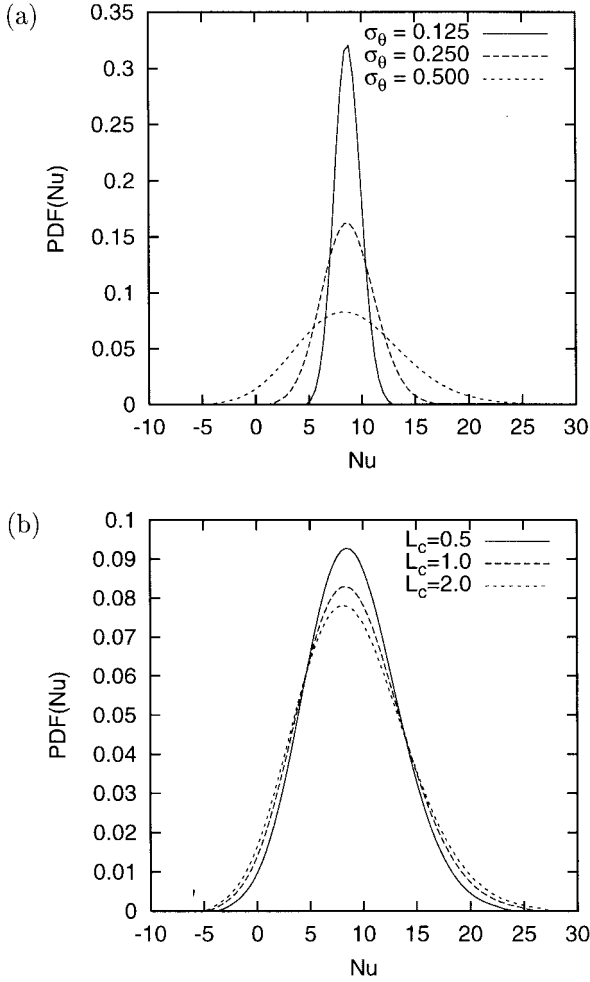


**FIG. 25.** PDFs of the Nusselt number computed from the spectral simulations using  $N_{\text{KL}} = 6$  and  $N_{\text{O}} = 2$ : (a)  $L_c = 1$  and  $\sigma_\theta = 0.125, 0.25$ , and  $0.5$ ; (b)  $\sigma_\theta = 0.5$  and  $L_c = 0.5, 1$ , and  $2$ .

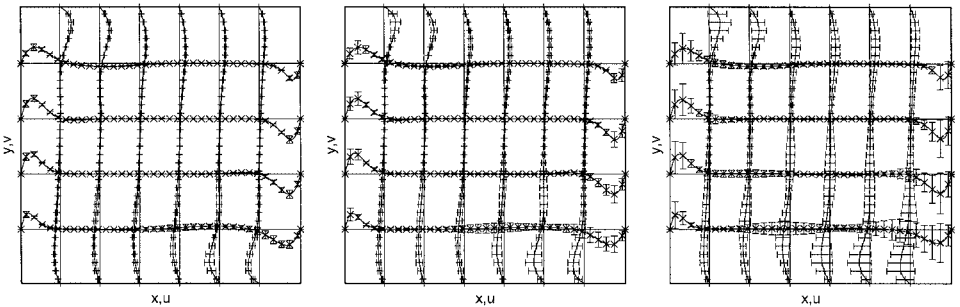


**FIG. 26.** Mean velocity profiles across the cavity for  $\sigma_\theta = 0.125$  (left),  $0.25$  (center), and  $0.5$  (right). The error bars correspond to 6 times the local standard deviation. The same scaling is used for all three plots. Spectral results with  $L_c = 1$ ,  $N_{\text{KL}} = 6$ , and  $N_{\text{O}} = 2$  are used.

uncertainty bars increase as  $\sigma_\theta$  increases. In particular, for  $\sigma_\theta = 0.5$  the uncertainty bars suggest that events with upward velocity near the cold wall become probable. In contrast, one observes that the mean flow field is not strongly affected by  $\sigma_\theta$ .

## 10. CONCLUSIONS

In this paper, the SPM [1] has been generalized to account for stochastic input data generated by a stochastic process. The Karhunen–Loève expansion is used to represent the stochastic input data. The dependence of the solution process on the random data is expressed in terms of the polynomial chaos system and the coefficients of the solution are determined using a weighted residual approach. The resulting stochastic formulation is incorporated into a finite-difference projection method, which results in an efficient stochastic solver.

The properties of the stochastic solver are analyzed in light of computed results for natural convection within a closed square cavity under stochastic temperature boundary conditions. In particular, the setup is used to examine the convergence properties of the spectral uncertainty representation scheme in terms of the number of KL modes and the order of the PC expansion. Computations are performed for a steady flow regime with Rayleigh number of  $10^6$ . For the selected conditions, the results indicate that the spectral representation converges rapidly, providing accurate results for a second-order expansion using as few as four KL modes. Numerical tests indicate that the CPU cost of the stochastic computations is essentially proportional to the number of modes used in the spectral representation, thus highlighting the efficiency of the stochastic model.

To verify the spectral predictions, stand-alone deterministic computations are performed and are used in conjunction with “nonintrusive” spectral projection approaches. Two variants of the NISP approach are implemented, one based on high-order Gauss–Hermite integration and the other on a Latin hypercube sampling strategy. Results obtained using Gauss quadrature are in excellent agreement with the spectral predictions, showing very small differences that are of the order of the spectral truncation errors. Predictions obtained using the Latin hypercube sampling scheme are also in agreement with the spectral predictions but exhibit differences that are an order of magnitude higher than those obtained using Gauss–Hermite quadrature. The verification study underscores the efficiency of the spectral computations, as the number of independent realizations needed to adequately represent the stochastic process is substantially higher than the corresponding number of PC modes. The analysis also shows that the nonintrusive approach based on Gauss–Hermite quadrature can be significantly more attractive than that using Latin hypercube sampling, at least for problems with a moderate number of stochastic dimensions.

The computations are used to quantify the effects of stochastic temperature conditions on the global heat transfer characteristics within the cavity. The results indicate that the mean Nusselt number,  $\overline{Nu}$ , is generally larger than  $Nu^0$ , the Nusselt number corresponding to the mean (uniform) temperature profile. In particular, the difference  $\overline{Nu} - Nu^0$  is found to increase quadratically with  $\sigma_\theta$ , the standard deviation of the stochastic temperature profile, but shows a weak dependence on the correlation length  $L_c$ . Meanwhile, the standard deviation of the Nusselt number exhibits an approximately linear dependence on  $\sigma_\theta$  and a more pronounced dependence on  $L_c$  than the mean Nusselt number.

So far, implementations of SPM have been restricted to flow conditions having relatively simple physical models, involving quadratic nonlinearities only. In other situations, more

complex physical models may arise that involve higher order nonlinearities. These result in additional computational challenges for the present approach, particularly regarding the implementation of the Galerkin scheme. Extensions that address these challenges in the context of chemically reacting flows are currently being developed.

## APPENDIX

A first-order expansion gives a spectral basis involving a set of  $P + 1 = N_{\text{KL}} + 1$  orthogonal polynomials:

$$\Psi_0 = 1, \quad \Psi_i = \xi_i \quad \text{for } i = 1, \dots, N_{\text{KL}} = P. \quad (39)$$

The governing equations for the zeroth-order velocity and temperature modes are

$$\frac{\partial \mathbf{u}_0}{\partial t} + \sum_{i=0}^{N_{\text{KL}}} \mathbf{u}_i \cdot \nabla \mathbf{u}_i = -\nabla p_0 + \frac{Pr}{\sqrt{Ra}} \nabla^2 \mathbf{u}_0, \quad (40)$$

$$\frac{\partial \theta_0}{\partial t} + \sum_{i=0}^{N_{\text{KL}}} \nabla \cdot (\mathbf{u}_i \theta_i) = \frac{1}{\sqrt{Ra}} \nabla^2 \theta_0. \quad (41)$$

For  $k = 1, \dots, N_{\text{KL}}$  the governing equations can be expressed as

$$\frac{\partial \mathbf{u}_k}{\partial t} + \mathbf{u}_0 \nabla \mathbf{u}_k + \mathbf{u}_k \nabla \mathbf{u}_0 = -\nabla p_k + \frac{Pr}{\sqrt{Ra}} \nabla^2 \mathbf{u}_k, \quad (42)$$

$$\frac{\partial \theta_k}{\partial t} + \nabla \cdot (\mathbf{u}_0 \theta_k + \mathbf{u}_k \theta_0) = \frac{1}{\sqrt{Ra}} \nabla^2 \theta_k. \quad (43)$$

Meanwhile, continuity gives

$$\nabla \cdot \mathbf{u}_k = 0, \quad k = 0, \dots, N_{\text{KL}}. \quad (44)$$

The velocity boundary conditions are given by

$$\mathbf{u}_k(\mathbf{x}, t) = 0 \quad \forall \mathbf{x} \in \partial\Omega, \quad \forall t \quad \text{and} \quad k = 0, \dots, N_{\text{KL}}, \quad (45)$$

while the scaled temperature boundary conditions are

$$\theta_0(x = 0, y) = 1/2, \quad \theta_0(x = 1, y) = -1/2, \quad (46)$$

$$\theta_k(x = 0, y) = 0, \quad \theta_k(x = 1, y) = \sqrt{\lambda_k} f_k(y) \quad \text{for } k = 1, \dots, N_{\text{KL}}, \quad (47)$$

and

$$\frac{\partial \theta_k}{\partial y} = 0 \quad \text{for } y = 0, 1 \quad \text{and} \quad k = 0, \dots, N_{\text{KL}}. \quad (48)$$

The first-order PC expansion thus leads to a set of  $N_{\text{KL}} + 1$  coupled momentum and heat equations and a set of  $N_{\text{KL}} + 1$  decoupled divergence constraints.

## ACKNOWLEDGMENTS

This work was supported by the Laboratory Directed Research and Development Program at Sandia National Laboratories, funded by the U.S. Department of Energy. Support was also provided by the Defense Advanced Research Projects Agency (DARPA) and Air Force Research Laboratory, Air Force Materiel Command, USAF, under agreement F30602-00-2-0612. The U.S. government is authorized to reproduce and distribute reprints for Governmental purposes notwithstanding any copyright annotation thereon. Computations were performed at the National Center for Supercomputer Applications.

## REFERENCES

1. O. P. Le Maître, O. M. Knio, H. N. Najm, and R. G. Ghanem, A stochastic projection method for fluid flow. I. Basic formulation, *J. Comput. Phys.* **173**, 480 (2001).
2. S. Wiener, The homogeneous chaos, *Am. J. Math.* **60**, 897 (1938).
3. R. H. Cameron and W. T. Martin, The orthogonal development of nonlinear functionals in series of Fourier–Hermite functionals, *Ann. Math.* **48**, 385 (1947).
4. A. J. Chorin, Hermite expansions in Monte-Carle computation, *J. Comput. Phys.* **8**, 472 (1971).
5. F. H. Maltz and D. L. Hitzl, Variance reduction in Monte Carlo computations using multi-dimensional Hermite polynomials, *J. Comput. Phys.* **32**, 345 (1979).
6. W. C. Meecham and D. T. Jeng, Use of the Wiener–Hermite expansion for nearly normal turbulence, *J. Fluid Mech.* **32**, 225 (1968).
7. S. C. Crow and G. H. Canavan, Relationship between a Wiener–Hermite expansion and an energy cascade, *J. Fluid Mech.* **41**, 387 (1970).
8. A. J. Chorin, Gaussian fields and random flow, *J. Fluid Mech.* **63**, 21 (1974).
9. R. G. Ghanem and P. D. Spanos, *Stochastic Finite Elements: A Spectral Approach* (Springer-Verlag, Berlin/New York, 1991).
10. G. De Vahl Davis and I. P. Jones, Natural convection in a square cavity: A comparison exercise, *Int. J. Numer. Methods Fluids* **3**, 227 (1983).
11. P. Le Quéré and T. Alziary de Roquefort, Computation of natural-convection in two-dimensional cavities with Tschebyscheff polynomials, *J. Comput. Phys.* **57**, 210 (1985).
12. P. Le Quéré, Accurate solution to the square thermally driven cavity at high Rayleigh number, *Comput. Fluids* **20**(1), 29 (1991).
13. D. R. Chenoweth and S. Paolucci, Natural convection in an enclosed vertical layer with large horizontal temperature differences, *J. Fluid Mech.* **169**, 173 (1986).
14. P. Le Quéré, R. Masson, and P. Perrot, A Chebyshev collocation algorithm for 2D non-Boussinesq convection, *J. Comput. Phys.* **103**, 320 (1992).
15. H. Paillere and P. Le Quéré, Modelling and simulation of natural convection flows with large temperature differences: A benchmark problem for low Mach number solvers, presented at 12th Seminar “Computational Fluid Dynamics” CEA/Nuclear Reactor Division, Saclay, France 2000.
16. M. Christon, P. Gresho, and S. Sutton, Computational predictability of natural convection flows in enclosure, in *Computational Fluid and Solid Mechanics*, edited by K. Bathe, Proceedings of First MIT Conference on Computational Fluid and Solid Mechanics (Elsevier, Amsterdam, 2001), pp. 1465–1468.
17. D. M. Christopher, Numerical prediction of natural convection flows in a tall enclosure, in *Computational Fluid and Solid Mechanics*, edited by K. Bathe, Proceedings of First MIT Conference on Computational Fluid and Solid Mechanics (Elsevier, Amsterdam, 2001), pp. 1469–1471.
18. G. Comini, M. Manzan, C. Nonino, and O. Saro, Finite element solutions for natural convection in a tall rectangular cavity, in *Computational Fluid and Solid Mechanics*, edited by K. Bathe, Proceedings of First MIT Conference on Computational Fluid and Solid Mechanics (Elsevier, Amsterdam, 2001), pp. 1472–1476.
19. G. Groce and M. Favero, Simulation of natural convection flow in enclosures by an unstaggered grid Finite volume algorithm, in *Computational Fluid and Solid Mechanics*, edited by K. Bathe, Proceedings of First MIT Conference on Computational Fluid and Solid Mechanics (Elsevier, Amsterdam, 2001), pp. 1477–1481.

20. P. M. Gresho and S. Sutton, 8:1 thermal cavity problem, in *Computational Fluid and Solid Mechanics*, edited by K. Bathe, Proceedings of First MIT Conference on Computational Fluid and Solid Mechanics (Elsevier, Amsterdam, 2001), pp. 1482–1485.
21. H. Johnston and R. Krasny, Computational predictability of natural convection flows in enclosures: A benchmark problem, in *Computational Fluid and Solid Mechanics*, edited by K. Bathe, Proceedings of First MIT Conference on Computational Fluid and Solid Mechanics (Elsevier, Amsterdam, 2001), pp. 1486–1489.
22. S.-E. Kim and D. Choudhury, Numerical investigation of laminar natural convection flow inside a tall cavity using a finite volume based Navier–Stokes solver, in *Computational Fluid and Solid Mechanics*, edited by K. Bathe, Proceedings of First MIT Conference on Computational Fluid and Solid Mechanics (Elsevier, Amsterdam, 2001), pp. 1490–1492.
23. T.-W. Pan and R. Glowinski, A projection/wave-like equation method for natural convection flows in enclosures, in *Computational Fluid and Solid Mechanics*, edited by K. Bathe, Proceedings of First MIT Conference on Computational Fluid and Solid Mechanics (Elsevier, Amsterdam, 2001), pp. 1493–1496.
24. A. G. Salinger, R. B. Lehoucq, R. P. Pawlowski, and J. N. Shadid, Understanding the 8:1 cavity problem via scalable stability analysis algorithms, in *Computational Fluid and Solid Mechanics*, edited by K. Bathe, Proceedings of First MIT Conference on Computational Fluid and Solid Mechanics (Elsevier, Amsterdam, 2001), pp. 1497–1500.
25. S. A. Suslov and S. Paolucci, A Petrov–Galerkin method for flows in cavities, in *Computational Fluid and Solid Mechanics*, edited by K. Bathe, Proceedings of First MIT Conference on Computational Fluid and Solid Mechanics (Elsevier, Amsterdam, 2001), pp. 1501–1504.
26. K. W. Westerberg, Thermally driven flow in a cavity using the Galerkin finite element method, in *Computational Fluid and Solid Mechanics*, edited by K. Bathe, Proceedings of First MIT Conference on Computational Fluid and Solid Mechanics (Elsevier, Amsterdam, 2001), pp. 1505–1508.
27. S. Xin and P. Le Quééré, An extended Chebyshev pseudo-spectral contribution to CPNCFE benchmark, in *Computational Fluid and Solid Mechanics*, edited by K. Bathe, Proceedings of First MIT Conference on Computational Fluid and Solid Mechanics (Elsevier, Amsterdam, 2001), pp. 1509–1513.
28. A. M. Lankhorst, *Laminar and Turbulent Natural Convection in Cavities; Numerical Modeling and Experimental Validation*, Ph.D. thesis (Delft University of Technology, 1991).
29. M. Loève, *Probability Theory* (Springer-Verlag, Berlin/New York, 1997).
30. M. Abramowitz and I. A. Stegun, *Handbook of Mathematical Functions* (Dover, New York, 1970).
31. O. M. Knio and R. G. Ghanem, *Polynomial Chaos Product and Moment Formulas: A User Utility*, Technical report (The Johns Hopkins University, Baltimore), to appear.
32. M. D. McKay, W. J. Conover, and R. J. Beckman, A comparison of three methods for selecting values of input variables in the analysis of output from a computer code, *Technometrics* **21**, 239 (1979).
33. R. Ghanem and S. Dham, Stochastic finite element analysis for multiphase flow in heterogeneous porous media, *Trans. Porous Media* **32**, 239 (1998).
34. R. Ghanem, Probabilistic characterization of transport in heterogeneous porous media, *Comput. Methods Appl. Mech. Eng.* **158**, 199 (1998).
35. A. J. Chorin, A numerical method for solving incompressible viscous flow problems, *J. Comput. Phys.* **2**, 12 (1967).
36. J. Kim and P. Moin, Application of a fractional-step method to the incompressible Navier–Stokes equations, *J. Comput. Phys.* **59**, 308 (1985).
37. M. S. Eldred, A. A. Giunta, S. F. Wojtkiewicz, B. G. van Bloemen Waanders, W. E. Hart, and M. P. Alleva, *DAKOTA, A Multilevel Parallel Object-Oriented Framework for Design Optimization, Parameter Estimation, Sensitivity Analysis, and Uncertainty Quantification, Version 3.0 Reference Manual*, Sandia Technical Report SAND02-XXXX, in preparation (Sandia National Laboratories, 2002); [http://endo.sandia.gov/DAKOTA/papers/Dakota\\_hardcopy.pdf](http://endo.sandia.gov/DAKOTA/papers/Dakota_hardcopy.pdf).
38. S. F. Wojtkiewicz, M. S. Eldred, R. V. Field, A. Urbina, and J. R. Red-Horse, *A Toolkit for Uncertainty Quantification in Large Computational Engineering Models, Meeting Paper 2001-1455* (AIAA Press, Washington, DC, 2001).
39. M. S. Eldred, *Optimization Strategies for Complex Engineering Applications*, Sandia Technical Report SAND98-0340 (Sandia National Laboratories, 1998).